A New Closure Assumption and Formulation Based on the Helmholtz Decomposition in the Generalized Velocity Track Display

Satoki Tsujino,[a,b] Takeshi Horinouchi,[a] and Udai Shimada,[b]

[a] *Faculty of Environmental Earth Science, Hokkaido University, Sapporo, Hokkaido, Japan*

[b] *Department of Typhoon and Severe Weather Research, Meteorological Research Institute, Tsukuba, Ibaraki, Japan*

Corresponding author: Satoki Tsujino, satoki@gfd-dennou.org

ABSTRACT: Doppler weather radars are powerful tools for investigating the inner-core structure and intensity of tropical cyclones (TCs). The Doppler velocity can provide quantitative information on the vortex structure in the TCs. The Generalized Velocity Track Display (GVTD) technique has been used to retrieve the axisymmetric circulations and asymmetric tangential flows in the TCs from ground-based single-Doppler radar observations. GVTD can have limited applicability to asymmetric vortices due to the closure assumption of no asymmetric radial flows. The present study proposes a new closure formulation that includes asymmetric radial flows, based on the Helmholtz decomposition. Here it is assumed that the horizontal flow is predominantly rotational and expressed with a streamfunction, but limited inclusion of wavenumber-1 divergence is available. Unlike the original GVTD, the decomposition introduces consistency along radius by requiring to solve equations simultaneously. The new approach, named GVTD-X, is applied to analytical vortices and a real TC with asymmetric structures. This approach makes the retrieval of axisymmetric flow relatively insensitive to the contamination from asymmetric flows and the error in the storm center locations. For an analytical vortex with a wavenumber-2 asymmetry, the maximum relative error of the axisymmetric tangential wind retrieved by GVTD-X is less than 2% at the radius of the maximum wind speed. In practical applications, errors can be evaluated by comparing results for different maximum wavenumbers. When applied to a real TC, GVTD-X largely suppressed an artificial periodic fluctuation that occurs in GVTD from the aliasing of the neglected asymmetric radial flows.

SIGNIFICANCE STATEMENT: The Generalized Velocity Track Display (GVTD) used to estimate circulations in tropical cyclones (TCs) with single-Doppler weather radars can have limited applicability to strongly asymmetric TCs due to the assumption of no asymmetric radial winds in the retrieval formulations. The present study proposes a new closure allowing asymmetric radial winds in GVTD. The relative error of the axisymmetric tangential wind in an asymmetric perfect vortex from the new approach is less than 2% at the radius of the maximum wind speed. In applying to a real TC with an elliptical eyewall, we found that the new approach can largely suppress an artificial evolution of the tangential winds in the original GVTD retrieval.

Keywords: Tropical cyclone, Doppler weather radar, Typhoon, Hurricane, Mesoscale meteorology

1. Introduction

Doppler weather radar can capture wind fields in areas with water condensates (i.e., around precipitation clouds). It is a powerful tool for the investigation of dynamics and kinematic structure in mesoscale systems such as tropical cyclones (TCs). In the North Atlantic, airborne Doppler radars have been used to reveal the three-dimensional wind fields in field campaigns of TCs, although the frequency of the observation is limited due to flight limitations (e.g., Houze et al. 2006, 2007; Bell et al. 2012). In contrast, ground-based Doppler radars cannot be deployed, but they can be operated continuously over time to capture the temporal evolution of the TCs. The high-frequency observations with them have been used to investigate the evolution of the circulation, vortex Rossby waves (VRWs), and asymmetric eyewall in the TC inner core (e.g., Muramatsu 1986; Shimada et al. 2018; Shimada and Horinouchi 2018; Cha et al. 2020; Dai et al. 2021).

The Doppler velocity from the ground-based single radar observations captures only the velocity component along the radar beam. This intrinsic limitation makes the retrieval of complete wind fields from single radar observations unavailable. Therefore, to estimate wind fields, assumptions suitable to observational targets are needed.

In the context of TC studies, Lee et al. (1999) developed the ground-based velocity track display (GBVTD). The GBVTD technique is to estimate both symmetric and asymmetric tangential winds as well as the symmetric component of radial wind in a vortex by the Fourier decomposition of the Doppler velocity $\mathcal{V}_d$ for a nonlinear angle ψ which is dependent on both azimuths with respect to the vortex center and the radar location. On the basis of the retrieved axisymmetric circulations, angular momentum, vertical vorticity, and pressure perturbation associated with the vortex can be also calculated (Lee et al. 2000; Lee and Wurman 2005; Lee and Bell 2007). The GBVTD technique has several limitations. The use of the nonlinear angle leads to the distortion of asymmetric flows and narrow retrieval area ($r < R_T$; r and R_T are the radius from the vortex center and the distance between the Doppler radar location and the vortex center, respectively). The closure assumption of GBVTD neglects asymmetric radial winds, which can degrade the retrieval of tangential winds (e.g., Lee et al. 2006). Murillo et al. (2011) showed a systematic difference of 6 m s^{-1} in the axisymmetric tangential wind between the single-Doppler radar retrieval by the GBVTD method and dual-Doppler radar retrieval at around the radius of maximum wind speed (RMW) in Hurricane Danny (1997).

Jou et al. (2008, J08) resolved the limitations due to the use of the nonlinear angle by simply using the azimuth with respect to the vortex center linear angle and the Fourier decomposition of a new variable $\mathcal{V}_d R_D / R_T$ for the linear angle, where R_D is the distance from the radar location to the target (Generalized VTD; GVTD). The GVTD technique allows us to apply the Doppler velocity retrieval beyond the radius of R_T, and it improves the accuracy of the retrieved circulations.

Cha and Bell (2021) validated the GVTD retrieval from the single-Doppler radar observations with the airborne dual-Doppler radar retrieval in Hurricane Matthew (2016), and reduced retrieval errors due to translation of the vortex by improving the formulations of the horizontally uniform winds in the GVTD method.

In regions that TCs often approach, such as the US, Japan, Taiwan, China, and the Philippines, observation networks by ground-based Doppler radars have been established with high-frequency volume scans or single plan-position-indicator (PPI) surveillance every 5 or 10 min. Thus, the detailed evolution of the TC circulation can be observed by the high-frequency Doppler radar networks. The GBVTD/GVTD techniques are useful to retrieve or estimate TC intensity from these operational ground-based Doppler radars. On the basis of the GBVTD technique, Shimada et al. (2016) estimated the intensity of 22 TCs approaching Japan from the ground-based single-Doppler radar observations and compared it with the best track from the Regional Specialized Meteorological Center (RSMC) Tokyo. They showed that the estimate of the GBVTD-based intensity is comparable to or better than those of Dvorak and satellite microwave-derived estimates.

The GBVTD/GVTD techniques have been used to not only assess the TC intensity but also to understand the dynamics of intensity and structure changes in TCs. Shimada et al. (2018) used the GBVTD to retrieve the inner-core circulation in Typhoon Goni (2015) from ground-based single-Doppler radar observations in the Okinawa Islands, and they investigated processes of the rapid intensification and contraction of the annular eyewall in Goni after the dissipation of the inner eyewall in an eyewall replacement cycle. They also discussed a key process with the absolute angular momentum budget diagnosed from the retrieved circulations. Cha et al. (2020) investigated asymmetric structure in the polygonal eyewall during the rapid intensification of Hurricane Michael (2018). They retrieved the asymmetric components of the hurricane tangential wind by the GVTD technique and compared the azimuthal propagating speed with the theory in the VRWs. Dai et al. (2021) used the GBVTD technique to examine the axisymmetric vorticity profiles and to investigate the evolution of the vortex structure in Typhoon Lekima (2019) with concentric eyewalls (CEs) before its landfall in China. They hypothesized a possibility of convection intensification in the outer eyewall associated with the outward propagation of the inner-eyewall VRWs.

It is known that the GBVTD and GVTD techniques sometimes yield large errors because of their closure assumption to set asymmetric radial winds to zero. This is because some Fourier components of asymmetric radial winds project onto the line-of-sight winds in the same way as the wavenumber-0 tangential winds do (see section 2c). Lee et al. (2006) reported that the retrieved axisymmetric tangential wind can have a relative error of about 20% at around the RMW through the GBVTD analysis for an idealized vortex with an elliptical eyewall which is composed of wavenumber-2 VRWs and an axisymmetric Rankine vortex. Proper evaluation of asymmetric winds would improve the axisymmetric tangential wind retrieval, but to naively retain them as variables make the retrieval equations unclosed (Lee et al. 1999). A single-component wind measurement does not resolve the two horizontal wind components, so some a priori restrictions are necessary.

In the present study, a new closure and different retrieval formulas from those in the GVTD technique are proposed to solve the problem by allowing non-zero radial winds. Here we make use of the nature that flows associated with TCs are predominantly rotational. In the new approach, on the basis of the Helmholtz decomposition theorem, asymmetric streamfunction and velocity potential (instead of the radial and tangential winds) are used to remove the assumption of no asymmetric radial winds in the GVTD technique. As will be shown in this paper, a single Doppler observation can be used to constrain the streamfunction that governs rotational flow. Moreover, non-zero asymmetric velocity potential is allowed to some extent, allowing divergent flow up to wavenumber 1. Another novelty is that, unlike GBVTD and GVTD that solve equations independently at each radius, the new approach uses simultaneous equations to solve for the entire radial grid points at once. The simultaneous solution introduces consistency along radius.

The accuracy of the retrieval in the new approach is assessed by being applied to analytical vortices. Moreover, the new approach and GVTD technique are applied to the retrieval of axisymmetric tangential winds in a real typhoon with elliptical eyewalls observed by an operational single-Doppler radar. We discuss the advantages and limitations of the new approach through a comparison with the GVTD results.

2. The new approach

The new approach in the present study follows most of the geometry and coordinate in GVTD. In contrast to GVTD, the new approach adopts 1) the closure assumptions to contain asymmetric radial winds by the separation of the horizontal winds between the rotational and divergent components based on the Helmholtz decomposition theorem and 2) the retrieval formulations based on the least-square method over the entire area from the radar observation. Thus, the new approach is named as the GVTD-X (from the pronunciation of GVTD-HeCs which is an abbreviation of GVTD with the Helmholtz-decomposition-based Closure assumptions).

a. Geometry and symbols

We introduce geometry setting and definition of wind components in the present study, which is somewhat different from those in the earlier studies (Lee et al. 1999, J08). A subtle but important difference is that we use the storm-motion velocity as the background velocity, which is justified in what follows.

As in Fig. 1, we set the x axis along the direction from the radar to the storm center for convenience. Suppose a point A at (r, θ), where r and θ are radius and azimuthal angle on the polar coordinate with the origin of the storm center "T". The unit vector along the line of sight from the radar to the point A is $\boldsymbol{k} = \frac{1}{\delta}(\rho + \cos\theta, \sin\theta)$ on the x-y coordinate, where $\delta \equiv D_A/r$ and $\rho \equiv R_T/r$.

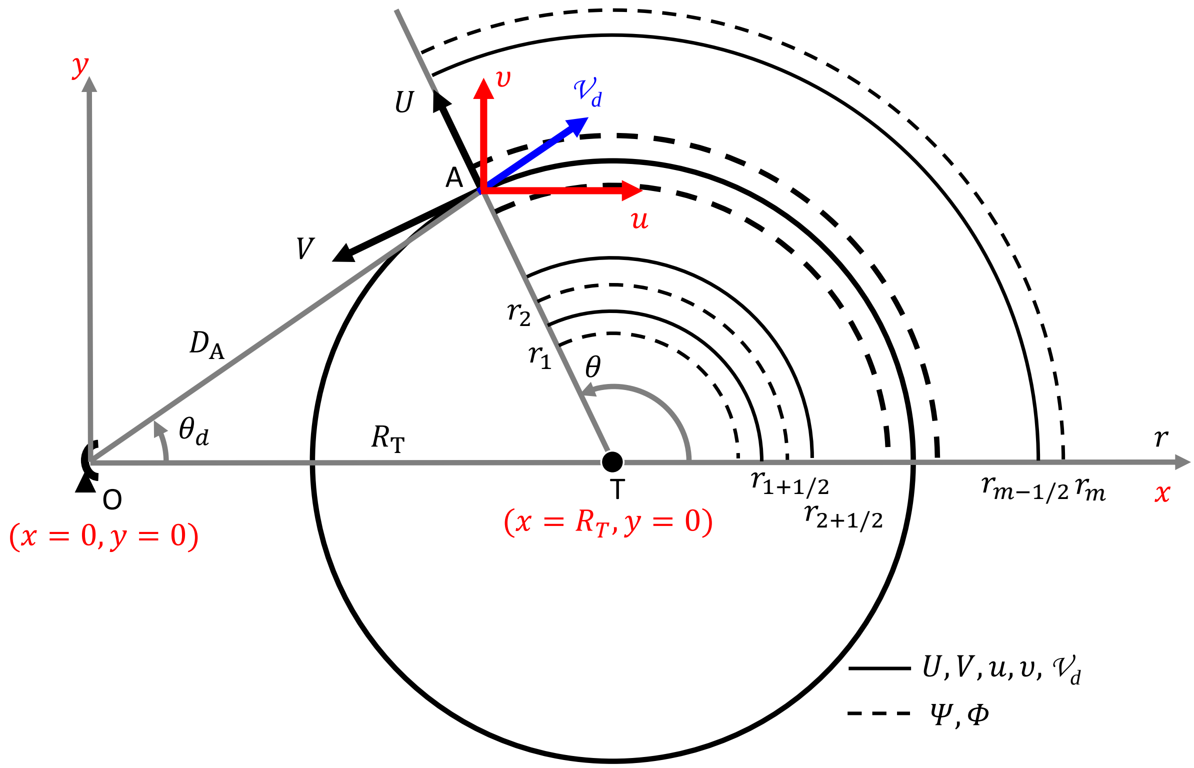

FIG. 1. Geometry and symbols in the new approach. A horizontal wind is presented by radial and tangential wind components (U and V) on the polar coordinates (r, θ) with the origin of the vortex center "T", and x and y components (u and v) on the Cartesian coordinates with the origin of the radar location at "O". The x and y axes are parallel and normal to the line OT, respectively. For the target located at the point "A", the Doppler velocity projected on the horizontal plane is represented by $\mathcal{V}_d$. Other symbols and lines are described in the main body.

D_A is the distance of the line OA in Fig. 1. The horizontal wind (u, v) in the x-y coordinate is related to the Doppler velocity $\mathcal{V}_d$ as follows:

$$\mathcal{V}_d \frac{\delta}{\rho} = u + \frac{1}{\rho}(u\cos\theta + v\sin\theta). \tag{1}$$

Following the conventional definition in most TC studies, u and v are expressed by the storm-motion velocity (u_S, v_S) and the storm-relative tangential (V) and radial (U) winds as,

$$\begin{bmatrix} u \\ v \end{bmatrix} = \begin{bmatrix} u_S + U\cos\theta - V\sin\theta \\ v_S + U\sin\theta + V\cos\theta \end{bmatrix}. \tag{2}$$

Equation (1) is then rewritten as

$$\mathcal{V}_d \frac{\delta}{\rho} = \mathcal{V}_S \frac{\delta}{\rho} + U\left(\frac{1}{\rho} + \cos\theta\right) - V\sin\theta, \tag{3}$$

where $\mathcal{V}_S \equiv \frac{\rho}{\delta} u_S + \frac{1}{\delta}(u_S\cos\theta + \upsilon_S\sin\theta)$ is the line-of-sight component of the storm motion from the radar.

Our wind separation in Eq. (2) is different from what is used in the original GBVTD and GVTD techniques, which use the mean flow $(u_M,\ \upsilon_M)$ as the background:

$$\begin{bmatrix} u \\ \upsilon \end{bmatrix} = \begin{bmatrix} u_M + \hat{U}\cos\theta - \hat{V}\sin\theta \\ \upsilon_M + \hat{U}\sin\theta + \hat{V}\cos\theta \end{bmatrix}. \tag{4}$$

Here, $(\hat{U},\ \hat{V})$ is the horizontal winds relative to the mean flow, which is rarely used in TC studies. Their methods retrieve $(\hat{U},\ \hat{V})$ rather than $(U,\ V)$. When $(u_M,\ \upsilon_M) \neq (u_S,\ \upsilon_S)$, $(\hat{U},\ \hat{V}) \neq (U,\ V)$. In the polar coordinate, their difference, which is a uniform flow, takes the form of a wavenumber-1 non-divergent and non-rotational flow in which tangential and radial winds have an equal amplitude. It does not have a wavnumber-0 component, but its mis-retrieval can bias the wavenumber-0 tangential flow. Note that asymmetric radial wind is set to zero in GBVTD and GVTD, so they cannot properly express uniform flow differences. Thus, the retrieved axisymmetric winds are different whether Eq. (3) or (4) is used.

b. A review of GVTD

In the GVTD technique of J08, $\mathcal{V}_d\delta/\rho$, $\hat{V}$ and $\hat{U}$ are expressed by the Fourier series on the θ coordinate:

$$\mathcal{V}_d \frac{\delta}{\rho} = A_0 + \sum_{k=1}^{N} A_k \cos(k\theta) + \sum_{k=1}^{N} B_k \sin(k\theta), \tag{5}$$

$$\hat{V} = \hat{V}_0 + \sum_{k=1}^{N-1} \hat{V}_{C,k} \cos(k\theta) + \sum_{k=1}^{N-1} \hat{V}_{S,k} \sin(k\theta), \tag{6}$$

$$\hat{U} = \hat{U}_0 + \sum_{k=1}^{N-1} \hat{U}_{C,k} \cos(k\theta) + \sum_{k=1}^{N-1} U_{S,k} \sin(k\theta), \tag{7}$$

where A_k ($\hat{V}_{C,k}$, $\hat{U}_{C,k}$) and B_k ($\hat{V}_{S,k}$, $\hat{U}_{S,k}$) are the cosine and sine components of $\mathcal{V}_d\delta/\rho$ (V, U) for the azimuthal wavenumber$-k$, respectively. In substituting Eqs. (5), (6), and (7) into Eq. (1), a set of simultaneous equations is established from the amplitude in each azimuthal wavenumber:

$$u_M = A_0 - \frac{1}{\rho}\hat{U}_0 + \frac{1}{2}\hat{V}_{S,1} - \frac{1}{2}\hat{U}_{C,1}, \tag{8}$$

$$\hat{V}_0 = -B_1 - B_3 + \frac{1}{\rho}\left[-v_M + \hat{U}_{S,1} + \hat{U}_{S,3}\right] + \hat{U}_{S,2}, \tag{9}$$

$$\hat{U}_0 = \frac{A_0 + A_1 + A_2 + A_3 + A_4}{1 + (1/\rho)} - \hat{U}_{C,1} - \hat{U}_{C,2} - \hat{U}_{C,3} - u_M, \tag{10}$$

$$\hat{V}_{S,k} = 2A_{k+1} - 2\frac{1}{\rho}\hat{U}_{C,k+1} + \hat{V}_{S,k+2} - \hat{U}_{C,k+2} - \hat{U}_{C,k}, \tag{11}$$

$$\hat{V}_{C,k} = -2B_{k+1} + \hat{V}_{C,k+2} + \hat{U}_{S,k} + \hat{U}_{S,k+2} + 2\frac{1}{\rho}\hat{U}_{S,k+1}. \tag{12}$$

u_M and v_M are the Cartesian x- and y-components of the mean flow (parallel and normal to the line between the radar and the vortex center), respectively (Fig. 1). For any truncating wavenumber N, the total number of the simultaneous equations is always less than the total number of the unknown variables. It means that a closure assumption is required to get the unique solution. Lee et al. (1999) and J08 assumed that all of the radial components of asymmetric flows associated with the vortex will be much smaller than others (i.e., $\hat{U}_{C,k} = \hat{U}_{S,k} = 0$). If they are actually non-zero, to neglect them in Eqs. (9) and (10) biases the retrieval of the axisymmetric velocities $\hat{V}_0$ and $\hat{U}_0$; this effect can be understood as an aliasing due to incorrect assumption. Thus, the assumption can be an obstacle to the application of the GBVTD and GVTD methods to TCs with significant asymmetries such as elliptical or polygonal eyewall. Even for an axisymmetric vortex advected by a mean flow, to assume $\hat{U}_{C,1} = \hat{U}_{S,1} = 0$ biases its flow retrieval if the mean flow, whether prescribed or retrieved, has an error, since the error induces non-zero wavenumber-1 components, such as the sensitivity experiments of the VM series in J08.

c. Formulation of the new method

In contrast to the closure assumption in GBVTD and GVTD, we attempt to include non-negligible asymmetric radial wind components in the closure of the new method. From Eq. (3), the Doppler velocity $\mathcal{V}_d'$ of a storm-relative horizontal wind $\mathbf{V}$ can be expressed as follows:

$$\mathcal{V}_d'\delta \equiv (\mathcal{V}_d - \mathcal{V}_S)\,\delta = -V\rho\sin\theta + U\rho\cos\theta + U. \tag{13}$$

On the basis of the Helmholtz decomposition theorem, the storm-relative wind $\mathbf{V}$ can be decomposed into the rotating component ($\mathbf{V}_{\mathrm{rot}}$), divergent component ($\mathbf{V}_{\mathrm{div}}$), and non-rotating and non-divergent component over the entire domain ($\mathbf{V}_{\mathrm{non}}$):

$$\mathbf{V} = \mathbf{V}_{\mathrm{non}} + \mathbf{V}_{\mathrm{rot}} + \mathbf{V}_{\mathrm{div}}. \tag{14}$$

The decomposition can be expressed by the streamfunction $\Phi(r,\theta)$ for $\mathbf{V}_{\mathrm{rot}} + \mathbf{V}_{\mathrm{non}}$ and the velocity potential $\Psi(r,\theta)$ for $\mathbf{V}_{\mathrm{div}}$:

$$V_{\mathrm{rot}} + V_{\mathrm{non}} = -\frac{\partial\Phi}{\partial r}, \tag{15}$$

$$U_{\mathrm{rot}} + U_{\mathrm{non}} = \frac{\partial\Phi}{r\partial\theta}, \tag{16}$$

$$V_{\mathrm{div}} = -\frac{\partial\Psi}{r\partial\theta}, \tag{17}$$

$$U_{\mathrm{div}} = -\frac{\partial\Psi}{\partial r}. \tag{18}$$

where $V_{\mathrm{rot}} + V_{\mathrm{non}}$, $U_{\mathrm{rot}} + U_{\mathrm{non}}$ are tangential and radial components of $\mathbf{V}_{\mathrm{rot}} + \mathbf{V}_{\mathrm{non}}$, and V_{div}, U_{div} are tangential and radial components of $\mathbf{V}_{\mathrm{div}}$. Note that globally non-rotating and non-divergent flow can be expressed with streamfunction and/or velocity potential. To make the decomposition unique, we express such flow exclusively with the streamfunction. Φ and Ψ are expressed by the Fourier expansion along the azimuth (θ):

$$\Phi(r,\,\theta) = \Phi_0(r) + \sum_{k=1}^{N}\left[\Phi_{S,k}(r)\sin(k\theta) + \Phi_{C,k}(r)\cos(k\theta)\right], \tag{19}$$

$$\Psi(r,\,\theta) = \Psi_0(r) + \sum_{k=1}^{L}\left[\Psi_{S,k}(r)\sin(k\theta) + \Psi_{C,k}(r)\cos(k\theta)\right], \tag{20}$$

where N and L are the truncating wavenumbers. Thus, Eqs. (15) to (18) can be expressed as follows:

$$V_{\mathrm{rot}} + V_{\mathrm{non}} = V_0(r) - \sum_{k=1}^{N} \left[\frac{\partial \Phi_{S,k}}{\partial r} \sin(k\theta) + \frac{\partial \Phi_{C,k}}{\partial r} \cos(k\theta) \right], \tag{21}$$

$$U_{\mathrm{rot}} + U_{\mathrm{non}} = \frac{1}{r} \sum_{k=1}^{N} \left\{ k \left[\Phi_{S,k}(r) \cos(k\theta) - \Phi_{C,k}(r) \sin(k\theta) \right] \right\}, \tag{22}$$

$$V_{\mathrm{div}} = -\frac{1}{r} \sum_{k=1}^{L} \left\{ k \left[\Psi_{S,k}(r) \cos(k\theta) - \Psi_{C,k}(r) \sin(k\theta) \right] \right\}, \tag{23}$$

$$U_{\mathrm{div}} = U_0(r) - \sum_{k=1}^{L} \left[\frac{\partial \Psi_{S,k}}{\partial r} \sin(k\theta) + \frac{\partial \Psi_{C,k}}{\partial r} \cos(k\theta) \right], \tag{24}$$

where

$$V_0 \equiv -\frac{\partial \Phi_0}{\partial r}, \quad U_0 \equiv -\frac{\partial \Psi_0}{\partial r}. \tag{25}$$

To ensure that $\mathbf{V}_{\mathrm{non}}$ is held exclusively in Φ, we relate Ψ to divergence D as follows:

$$\Psi_k = \int_0^\infty r' G_k(r;r') D_{S,k}(r') dr' \sin(k\theta) + \int_0^\infty r' G_k(r;r') D_{C,k}(r') dr' \cos(k\theta), \quad (k > 0), \tag{26}$$

$$D = \sum_{k=1}^{L} \left[D_{S,k}(r) \sin(k\theta) + D_{C,k}(r) \cos(k\theta) \right], \tag{27}$$

where G_k is the radial Green function (i.e., the impulse response in the Poisson equation on the $r-\theta$ coordinates) for wavenumber k:

$$G_k(r;r') = -\frac{1}{2k} \begin{cases} (r/r')^k, & (r \le r') \\ (r'/r)^k, & (r > r') \end{cases}, \quad (k \in \mathbb{N}). \tag{28}$$

Equation (26) is derived in Appendix A. If $D_{S,k} = D_{C,k} = 0$, $\Psi_k = 0$, and thus $U_{\mathrm{div}} = V_{\mathrm{div}} = 0$. Therefore, U_{non} and V_{non} are exclusively represented by Φ.

From Eqs. (14) and (21)–(25), $\mathcal{V}_d'$ in Eq. (13) is

$$\begin{aligned}\mathcal{V}_d'\delta = &\left\{\sum_{k=0}^{N}\left[\frac{\partial\Phi_{S,k}}{\partial r}\sin(k\theta)+\frac{\partial\Phi_{C,k}}{\partial r}\cos(k\theta)\right]\right.\\&\left.+\frac{1}{r}\sum_{k=1}^{L}\left\{k\left[\Psi_{S,k}(r)\cos(k\theta)-\Psi_{C,k}(r)\sin(k\theta)\right]\right\}\right\}\rho\sin\theta\\&+\left\{\frac{1}{r}\sum_{k=1}^{N}\left\{k\left[\Phi_{S,k}(r)\cos(k\theta)-\Phi_{C,k}(r)\sin(k\theta)\right]\right\}\right.\\&\left.-\sum_{k=0}^{L}\left[\frac{\partial\Psi_{S,k}}{\partial r}\sin(k\theta)+\frac{\partial\Psi_{C,k}}{\partial r}\cos(k\theta)\right]\right\}(1+\rho\cos\theta).\end{aligned}\tag{29}$$

To discretize the system, we employ a radially staggered grid as shown in Fig. 1. Suppose that the Doppler velocity $\mathcal{V}_d^{\mathrm{o}}$ is obtained at the grid points $(r_{i+1/2},\ \theta_j),\ (i=1,\cdots,m-1,\ j=1,\cdots,n)$, where the half-integer radii are shown by the black-solid arcs in Fig. 1, and m and n are the numbers of the radial and azimuthal grid points where Doppler velocities are defined, respectively. The radial and azimuthal grid intervals Δr and $\Delta\theta$, respectively, are set uniform; non-uniform grid spacing along r is treated in section 2f. The discretized Φ and D are allocated to the integer-radii grid points $(r_i,\ \theta_j),\ (i=1,\cdots,m,\ j=1,\cdots,n)$ as shown by the black-dashed arcs in Fig. 1. The discretized form of Eq. (29) can be expressed as follows:

$$\begin{aligned}\mathcal{V}_{d,i+1/2,j}'\delta \equiv &\left\{-V_{0,i+1/2}+\sum_{k=1}^{N}\left[\frac{\Phi_{S,k,i+1}-\Phi_{S,k,i}}{\Delta r}\sin(k\theta_j)+\frac{\Phi_{C,k,i+1}-\Phi_{C,k,i}}{\Delta r}\cos(k\theta_j)\right]\right.\\&\left.+\frac{\Delta r}{r_{i+1/2}}\sum_{k=1}^{L}\sum_{l=1}^{m-1}\left\{\varepsilon_l k r_l' G_{k,i+1/2,l}\left[D_{S,k,l}\cos(k\theta_j)-D_{C,k,l}\sin(k\theta_j)\right]\right\}\right\}\\&\times\rho_{i+1/2}\sin\theta_j\\&+\left\{U_{0,i+1/2}-\Delta r\sum_{k=1}^{L}\sum_{l=1}^{m-1}\left\{\varepsilon_l r_l'\frac{G_{k,i+1,l}-G_{k,i,l}}{\Delta r}\left[D_{S,k,l}\sin(k\theta_j)+D_{C,k,l}\cos(k\theta_j)\right]\right\}\right.\\&\left.+\sum_{k=1}^{N}\left[k\frac{\Phi_{S,k,i+1}+\Phi_{S,k,i}}{2r_{i+1/2}}\cos(k\theta_j)-k\frac{\Phi_{C,k,i+1}+\Phi_{C,k,i}}{2r_{i+1/2}}\sin(k\theta_j)\right]\right\}\\&\times(1+\rho_{i+1/2}\cos\theta_j).\end{aligned}\tag{30}$$

Here, we neglect D at $r > r_{m-1/2}$. This is because the flow field associated with it is non-divergent in the observational area of $r \leq r_{m-1/2}$, so it is expressed by Φ. We defined Φ and D at half-integer radii as $z_{i+1/2} = \frac{z_i + z_{i+1}}{2}$, where z is any variable. For $k = 0$, we do not use Φ and D but define V_0 and U_0 directly at half-integer radii. An integral operation of a variable z arising from Eq. (26) is assessed in Eq. (30) as follows:

$$\int_{r_1}^{r_m} z(r)dr \approx \frac{\Delta r}{2}\left[z_1 + z_{m-1} + 2\sum_{i=2}^{m-2} z_i\right] = \Delta r \sum_{i=1}^{m-1} \varepsilon_i z_i, \quad \varepsilon_i \equiv \begin{cases} 1/2, & (i = 1, m-1) \\ 1, & \text{(otherwise)} \end{cases}$$

The first derivative of a variable z with r at $r_{i+1/2}$ in Eq. (30) is assessed by the second-order centred difference approximation:

$$\left.\frac{dz}{dr}\right|_{i+1/2} \approx \frac{z_{i+1} - z_i}{\Delta r}.$$

In GVTD, retrieval is independently done for each radius. However, Eq. (30) combines all radii, so its retrieval needs to be done simultaneously. It introduces consistency across the radii.

We solve Eq. (30) by using the least-square method with respect to $\mathcal{V}_d'\delta$, so the residual $\mathcal{R}$ is expressed as,

$$\mathcal{R} \equiv \sum_{j=1}^{n}\sum_{i=1}^{m-1}\left[\mathcal{V}_d'^{\mathrm{o}}\delta - \mathcal{V}_d'\delta\right]_{i+1/2,j}^2, \tag{31}$$

where $\mathcal{V}_d'^{\mathrm{o}} \equiv \mathcal{V}_d^{\mathrm{o}} - \mathcal{V}_S$. Based on the least-square method, the minimum of $\mathcal{R}$ is searched. Equation (30) can be expressed abstractly in the form of

$$\mathcal{V}_{d,i+1/2,j}'\delta = \sum_{l=1}^{P} \alpha_l f_{l,i+1/2,j}, \tag{32}$$

where P is the total number of the unknown variables (α_l), which is the collection of the entire unknown variables on the right-hand-side of Eq. (30). $f_{l,i+1/2,j}$ is the coefficient of α_l, which is a sparse matrix with i and j. The set of the unknown variables to minimize $\mathcal{R}$ satisfies the following conditions:

$$\frac{\partial \mathcal{R}}{\partial \mathbf{x}} = \mathbf{0}, \tag{33}$$

$$\mathbf{x} \equiv \left[\alpha_1, \cdots, \alpha_l, \cdots, \alpha_P\right]^T. \tag{34}$$

For $\partial\mathcal{R}/\partial\alpha_l$ in Eq. (33),

$$\begin{aligned}\frac{\partial\mathcal{R}}{\partial\alpha_l} &= \sum_{i,j} f_{l,i+1/2,j}\left[\sum_{q=1}^{P}\alpha_q f_{q,i+1/2,j} - \mathcal{V}'^{\mathrm{o}}_{d,i+1/2,j}\delta\right] \\ &= \sum_{q=1}^{P}\left[\alpha_q \sum_{i,j} f_{q,i+1/2,j} f_{l,i+1/2,j} - \sum_{i,j} f_{l,i+1/2,j}\mathcal{V}'^{\mathrm{o}}_{d,i+1/2,j}\delta\right] = 0. \end{aligned} \tag{35}$$

From Eqs. (33) and (35), we obtain a set of the linear simultaneous equations for α_l, $(l = 1, \cdots, P)$:

$$A\mathbf{x} = \mathbf{b}, \tag{36}$$

where

$$A \equiv \begin{bmatrix} a_{1,1} & \cdots & a_{1,P} \\ \vdots & \ddots & \vdots \\ a_{P,1} & \cdots & a_{P,P} \end{bmatrix}, \quad a_{l,q} \equiv \sum_{i,j} f_{l,i+1/2,j} f_{q,i+1/2,j}, \tag{37}$$

$$\mathbf{b} \equiv [b_1, \cdots, b_l, \cdots, b_P]^T, \quad b_l \equiv \sum_{i,j} f_{l,i+1/2,j}\mathcal{V}'^{\mathrm{o}}_{d,i+1/2,j}\delta. \tag{38}$$

If the matrix A is regular, the unknown variables α_l have a unique set of solutions. However, the matrix A can be irregular, so additional constraints are required to avoid the irregularity.

Let's consider a set of linear constraints for $\mathbf{x}$ to avoid the irregularity formally:

$$B\mathbf{x} = \mathbf{y}, \tag{39}$$

where B and $\mathbf{y}$ are known matrix and vector, respectively. The optimization problem Eq. (33) with the equality constraint Eq. (39) can be solved with the method of Lagrange multiplier:

$$\frac{\partial\mathcal{L}}{\partial\mathbf{x}} = \mathbf{0}, \tag{40}$$

$$\frac{\partial\mathcal{L}}{\partial\boldsymbol{\lambda}} = \mathbf{0}, \tag{41}$$

$$\mathcal{L}(\mathbf{x},\ \boldsymbol{\lambda}) \equiv \mathcal{R} + 2\boldsymbol{\lambda}^T(B\mathbf{x} - \mathbf{y}), \tag{42}$$

where $\mathcal{L}$ is a Lagrangian function, and $\boldsymbol{\lambda}$ is a vector consisted of Lagrange multipliers. Although Eqs. (40) and (41) are numerically solved in a practical manner, we briefly explain the analytical solution ($\mathbf{x}^*$) of $\mathbf{x}$ for Eqs. (40) and (41):

$$\mathbf{x}^* = A^{-1}\mathbf{b} + A^{-1}B^T \left[BA^{-1}B^T\right]^{-1} \left(\mathbf{y} - BA^{-1}\mathbf{b}\right). \tag{43}$$

The first term on the right-hand-side of Eq. (43) is identical to the solution for Eq. (36), which is the condition for $\mathbf{x}$ to minimize $\mathcal{R}$. The second term on the right-hand-side of Eq. (43) is the adjustment by the constraints (39). In the next section, specific formula of the constraints to avoid the irregularity are introduced.

d. Inherent ambiguity and closure

A single Doppler radar can measure only one wind component, so to retrieve two dimensional flow without any restriction is impossible. Suppose the homogeneous equation of Eq. (30) in which the left-hand-side is set to zero. If this homogeneous equation has a non-trivial solution, Eq. (30) or its least error version Eq. (33) is not uniquely solvable, leading to inherent ambiguity in the retrieval. Appendices B and C show that this is indeed the case; it occurs even when the number of azimuthal grid points is increased to infinity. Here we introduce a method to eliminate the non-trivial solution (or the inherent ambiguity) to make the problem solvable. The argument illuminates the interdependece among the Fourier components, which helps understand the behavior of GVTD and GBVTD like retrievals.

On the basis of the discussion in Appendices B and C, we propose closure assumptions to eliminate the ambiguity in the retrieval:

- The truncation wavenumber for Ψ is set to $L = 1$ in Eq. (20).
- $\Psi_{S,1}$ is also eliminated by setting $D_{S,1,l} = 0$ for all l.
- The non-trivial solution in $\Phi_{S,k}$ and $\Phi_{C,k}$ for the wavenumber k ($2 \le k \le N$), which is proportional to r^k, is eliminated by setting zero at the outermost radius:

$$\Phi_{C,k} = \Phi_{S,k} = 0, \quad (r = r_m). \tag{44}$$

We further require $\partial\Phi_{C,k}/\partial r = \partial\Phi_{S,k}/\partial r = 0$ at $r = r_{m-1/2}$, so we set

$$\Phi_{S,k,m} = \Phi_{S,k,m-1} = 0, \quad \Phi_{C,k,m} = \Phi_{C,k,m-1} = 0, \quad (2 \le k \le N). \tag{45}$$

Equation (45) means that all asymmetric components of not only non-trivial flows but also rotational winds for the wavenumber k vanish at $r_{m-1/2}$. Note that, if sufficient external information is somehow available, one can prescribe these values to non-zero. For example, the $k = 2$ ambiguity is associated with confluence/diffluence, which can exist in the environmental flow.

- The ambiguity at $k = 1$ can be treated similarly, but a remark is needed: $\Phi_{S,1}$ does not have non-trivial solutions, so it should not be constrained. The cosine part can also be constrained by $\Phi_{C,1,m} = \Phi_{C,1,m-1} = 0$, but it is recommended to prescribe non-zero values to them, if possible, as shown in the next subsection.

The above settings are necessary for accurate retrieval of Φ_0 and V_0 (Appendix C).

e. Constraints for $\Phi_{C,1}$

In section 2d, it is stated that $\Phi_{C,1}$ can be constrained by $\Phi_{C,1,m} = \Phi_{C,1,m-1} = 0$. In this case, the Cartesian y-component (perpendicular to the line between the radar and the vortex center) of the storm-relative mean winds at $r_{m-1/2}$,

$$dv_M \equiv \frac{1}{2\pi}\int_0^{2\pi} (v(r_{m-1/2}) - v_S)d\theta,$$

becomes identical to 0. This is because

$$dv_M \equiv \frac{1}{2\pi}\int_0^{2\pi} (U\sin\theta + V\cos\theta)\, d\theta = -\frac{1}{2}\left[\frac{\Phi_{C,1}}{r} + \frac{\partial\Phi_{C,1}}{\partial r}\right], \quad (r = r_{m-1/2}) \tag{46}$$

When the outermost radius $r_{m-1/2}$ is small enough (so that the storm-relative streamline around there is nearly closed), this is an adequate assumption. However, if dv_M is actually non-zero, to neglect it degrades the axisymmetric tangential-wind retrieval, as shown in what follows. This artifact is likely to occur when $r_{m-1/2}$ is large or the environmental shear is large. Since the wavenumber-0 retrieval is especially important, it is recommended to estimate dv_M and prescribe it in the retrieval, when possible.

From the structure of the wavenumber-1 ambiguity proportional to r [Eq. (C15)], Eq. (46) indicates that $\Phi_{C,1,m-1/2}/r_{m-1/2} = -dv_M$. Then, Eq. (C3) shows that there is a trade-off between $V_0 = -\partial\Phi_0/\partial r$ and $\rho^{-1}\Phi_{C,1}/r = -\rho^{-1}dv_M = -(r/R_T)dv_M$. Therefore, where $r \simeq R_T$, an error in dv_M biases the mean tangential wind retrieval nearly by the same amount. The effect is small if $r < R_T$, so retrieval near the center is less affected. One way to estimate dv_M is to use mean flow v_M from objective analysis, if $r_{m-1/2}$ is much larger than the inner-core radius:

$$dv_M = v_M - v_S. \tag{47}$$

f. Treatment of radius with insufficient sampling or unequally radial grids

So far, we have assumed that sufficient observational data are available at all radial grid points to constrain the streamfunction up to $k = N$. However, Doppler weather radar observations require precipitating hydrometeor, so data-missing can be severe at some radii, which typically occurs around the moat of TCs with CEs. This problem can be avoided by skipping radii where insufficient data are available. To do so is straightforward in GVTD in which retrieval is independent along radii. However, the new method does not allow data missing that makes Eq. (30), which is over multiple radii, unsolvable. This problem can be solved by removing the radii with insufficient sampling, named unused radii, from the radial grid point set, making it unequally spaced.

Let's consider equally spaced radial grid point set $(r_{i'+1/2}, i' = 1, 2, \cdots)$. If azimuthal sampling is insufficient at radii from $r_{i1+1/2}$ to $r_{i2+1/2}$ $(i1 \le i' \le i2)$, the radii are removed from the set, and grid indices are rearranged. Then, a new mid-point radius (r_i) is introduced as shown in Fig. 2:

$$r_i \equiv \frac{r_{i1} + r_{i2+1}}{2}, \quad r_{i-1/2} \equiv r_{i1-1/2}, \quad r_{i+1/2} \equiv r_{i2+3/2}. \tag{48}$$

In general, the new radius is not located on the original (i.e., equally radial) grids. The streamfunction and divergence are defined at the radius (r_i). Then, the velocities at the adjacent radii $(r_{i\pm 1/2})$ can be derived by using the parameters shown in Table 1. The velocities at the unused radii could

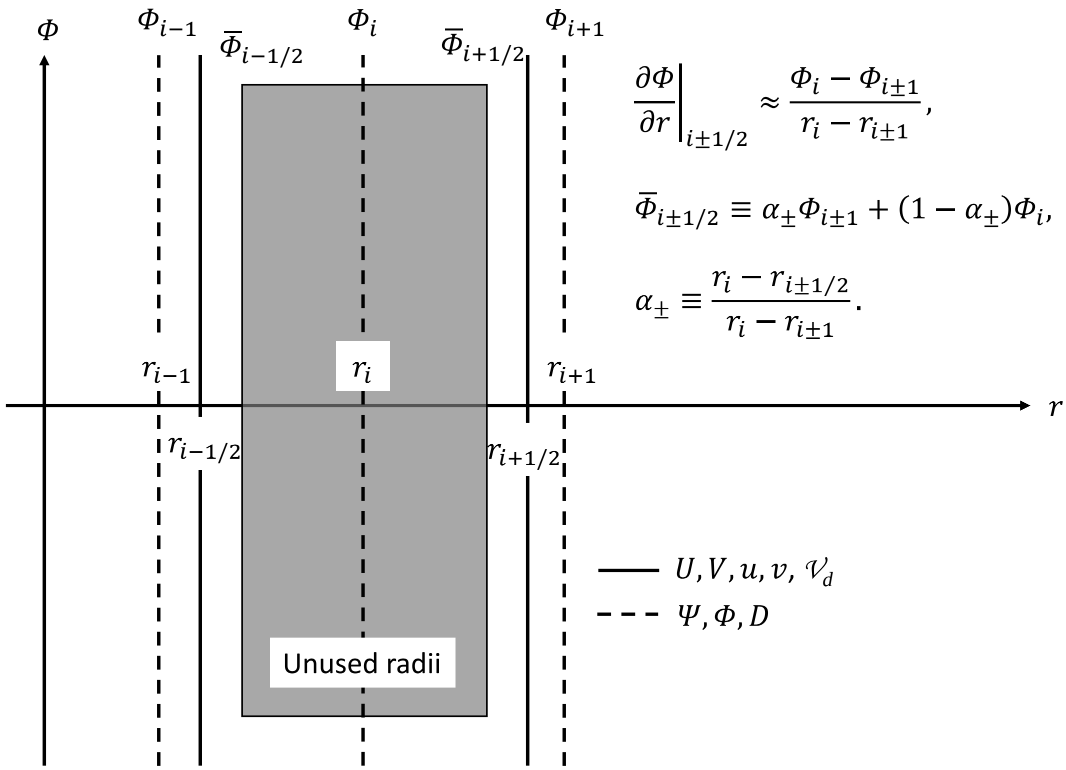

FIG. 2. A conceptual image for unused radii in a part of observations on the equally radial grids. The vertical solid (dashed) lines with black indicate radii at which velocities (streamfunction and divergence) are defined. Note that the index i indicates the order of the unequally radial grids after the removal of the unused radii on the equally radial grids. Adjusting symbols in the figure to the main body, $r_{i-1/2} \equiv r_{i1-1/2}$, $r_{i+1/2} \equiv r_{i2+3/2}$. The conceptual image can be also applied to observations on the unequally radial grids.

TABLE 1. At radii ($r_{i\pm1/2}$) in which velocities are defined, representation of parameters related to an arbitrary function $f(r_i) = f_i$ on the equally (unequally) radial grids in the middle (right) column. $\mu_\pm \equiv (r_i - r_{i\pm1/2})(r_i - r_{i\pm1})^{-1}$.

	Equal	Unequal
$f_{i\pm1/2}$	$\frac{f_{i\pm1}+f_i}{2}$	$\mu_\pm f_{i\pm1} + (1-\mu_\pm) f_i$
$\left.\frac{\partial f}{\partial r}\right\vert_{i\pm1/2}$	$\pm\frac{f_{i\pm1}-f_i}{\Delta r}$	$\frac{f_{i\pm1}-f_i}{r_{i\pm1}-r_i}$
$\int_0^\infty f dr$	$\Delta r \sum_{i=1}^{m} \varepsilon_i f_i$	$\sum_{i=1}^{m-1} (r_{i+1}-r_i)(f_{i+1}+f_i)/2$

be defined from the retrieval results, but we recommend not to do it by setting data missing there. That way, one can easily recognize data gap.

g. Use of multiple N and the error evaluation

We have formulated GVTD-X to use a single maximum wavenumber N, which is to be specified somehow. In practice, one can try retrievals for multiple values of N, as will be explored in section 4c. This will provide us with a guideline for choosing N and the error evaluation.

3. Application to analytical vortices

a. Structures of analytical vortices

Following Lee et al. (1999), J08, and Lee et al. (2006), GVTD-X is applied to two analytical vortices: 1) an axisymmetric Rankine vortex named AX-VORTEX (Figs. 3a-3c) and 2) an elliptical vortex that superposes a wavenumber-2 VRW on the AX-VORTEX named VRW2-VORTEX (Figs. 4a-4c). AX-VORTEX has the maximum wind speed of 50 m s^{-1} (= $V_{\max}$) at the RMW of 20 km (= $r_{\max}$):

$$V = V_{\max}\frac{r}{r_{\max}}, \qquad r \le r_{\max}, \tag{49}$$

$$V = V_{\max}\frac{r_{\max}}{r}, \qquad r > r_{\max}, \tag{50}$$

which is made by Eqs. (28) and (29) in Lee et al. (1999). VRW2-VORTEX is a non-divergent vortex with wavenumber-2 vorticity (ζ_2) confined within $r = 2r_{\max}$:

$$\zeta_2 = \begin{cases} (V_p/r_{\max})\cos[2(\theta+\theta_0)], & (r \le 2r_{\max}), \\ 0, & (r > 2r_{\max}). \end{cases} \tag{51}$$

where $V_p = 10$ m s^{-1}, and θ_0 is an additional phase. The wavenumber-2 components of the tangential and radial winds (V_2 and U_2) are constructed as follows, respectively:

$$\begin{aligned} V_2 &= -\frac{V_p}{r_{\max}}\left[\int_0^{2r_{\max}} r'\frac{\partial G_2}{\partial r}dr'\right]\cos[2(\theta+\theta_0)], \\ U_2 &= -\frac{V_p}{r_{\max}}r^{-1}\left[\int_0^{2r_{\max}} 2r'G_2 dr'\right]\sin[2(\theta+\theta_0)], \end{aligned} \tag{52}$$

where G_2 is the Green function for the wavenumber-2. The maxima of U_2 and V_2 are 5 m s^{-1} and 3 m s^{-1} at around the RMW, respectively. The integral and derivative for r in Eq. (52) are numerically

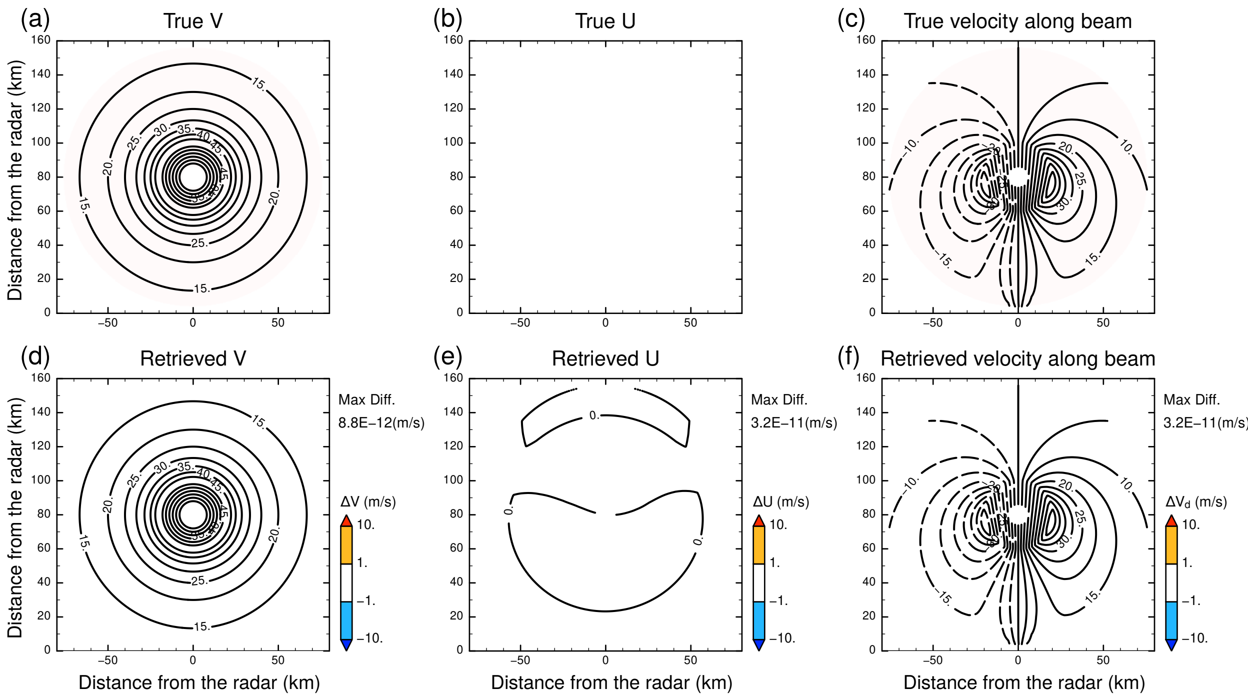

FIG. 3. Comparison of (left) tangential and (middle) radial winds and (right) Doppler velocity between the (top) true (i.e., analytical) vortex and (bottom) retrieval in AX-VORTEX (i.e., the axisymmetric Rankine vortex). The contour intervals for the tangential wind and Doppler velocity are every 5 m s^{-1}. The contours for the radial wind are 0 m s^{-1}, ±1 m s^{-1}, ±2 m s^{-1}, and ±4 m s^{-1}. The color shade (m s^{-1}) in the bottom panels means the difference between the true and retrieved vortices. The virtual radar is located at (0,0).

conducted to specify the vorticity field in the vortex.[1] The asymmetric streamfunctions, which are unknown variables in GVTD-X, can completely represent rotating winds (i.e., non-divergent vortices) in principle. Thus, GVTD-X can fully capture the asymmetric structure in VRW2-VORTEX, even the asymmetry of the radial winds. As with J08, we retrieve the flow patterns associated with these analytical vortices by GVTD-X from a virtual Doppler radar. The maximum (i.e., truncating) wavenumber of 3 for the streamfunction is used in the GVTD-X retrieval.

b. Results

Figure 3 shows the GVTD-X retrieval for AX-VORTEX. The projection of the retrieved circulations on the Doppler velocity is quantitatively consistent with the analytical profile (Figs. 3c and

[1]The radial structure of the wavenumber-2 winds expressed by Eq. (52) is similar to Eqs. (3)−(6) in Lee et al. (2006)

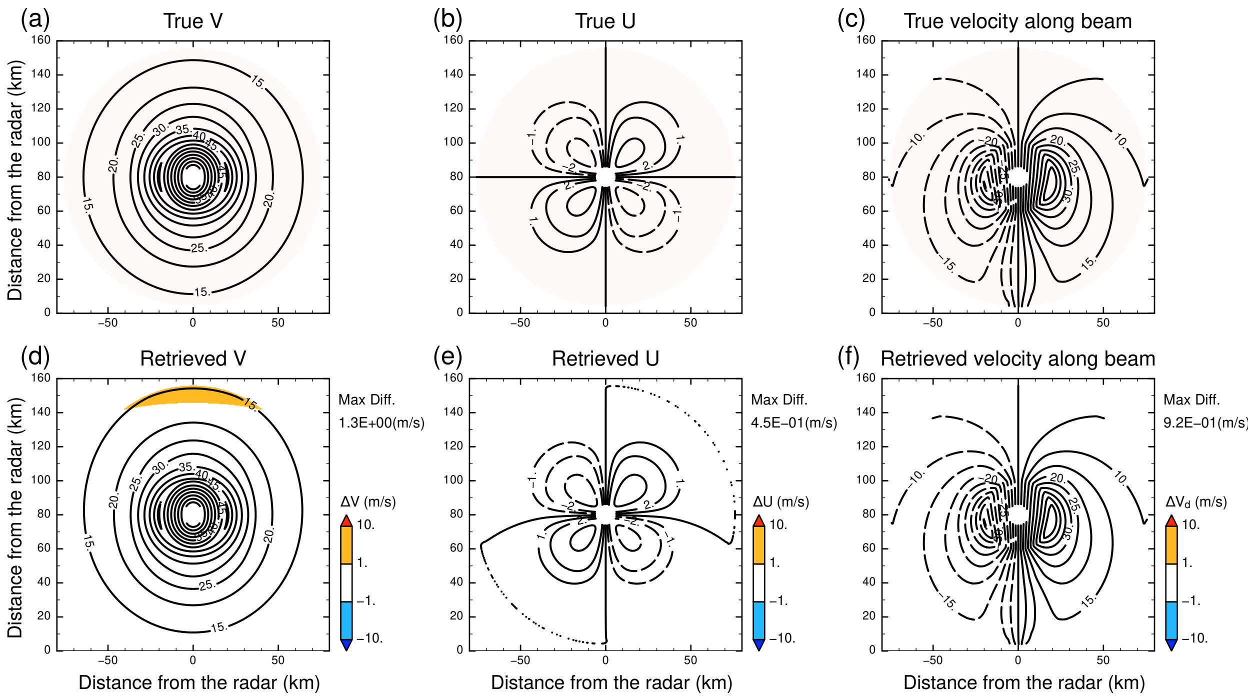

Fig. 4. As in Fig. 3, except for VRW2-VORTEX (i.e., the wavenumber-2 VRWs embedded in AX-VORTEX).

3f). The difference in the tangential wind between the analysis and retrieval is less than 1 m s^{-1} over the whole area (Figs. 3a and 3d). Note that AX-VORTEX has no radial flows (Figs. 3b and 3e).

Figure 4 shows the GVTD-X retrieval for VRW2-VORTEX. The projection of the retrieved circulations on the Doppler velocity is quantitatively consistent with the analytical profile (Figs. 4c and 4f). The difference in the tangential wind between the analytical and retrieved vortices is less than 1 m s^{-1} over a wide range from the center (Fig. 4d). A region where the difference is greater than 1 m s^{-1} exists near the outermost radius. The relatively large difference is mainly due to the constraint to eliminate asymmetric flows (the maxima of $V_2 = 0.55$ m s^{-1} and $U_2 = 0.33$ m s^{-1} in the analytical vortex) at the outermost radius [Eq. (45)]. The wavenumber-2 asymmetric radial flows can be mostly retrieved in GVTD-X (Figs. 4b and 4e) as we expect. We emphasize that the asymmetric radial flows can be reasonably captured in GVTD-X even if the artificial boundary conditions are given in the streamfunctions at the outermost radius. The asymmetries of the radial flows cannot be retrieved in the GBVTD/GVTD techniques due to their closure assumptions.

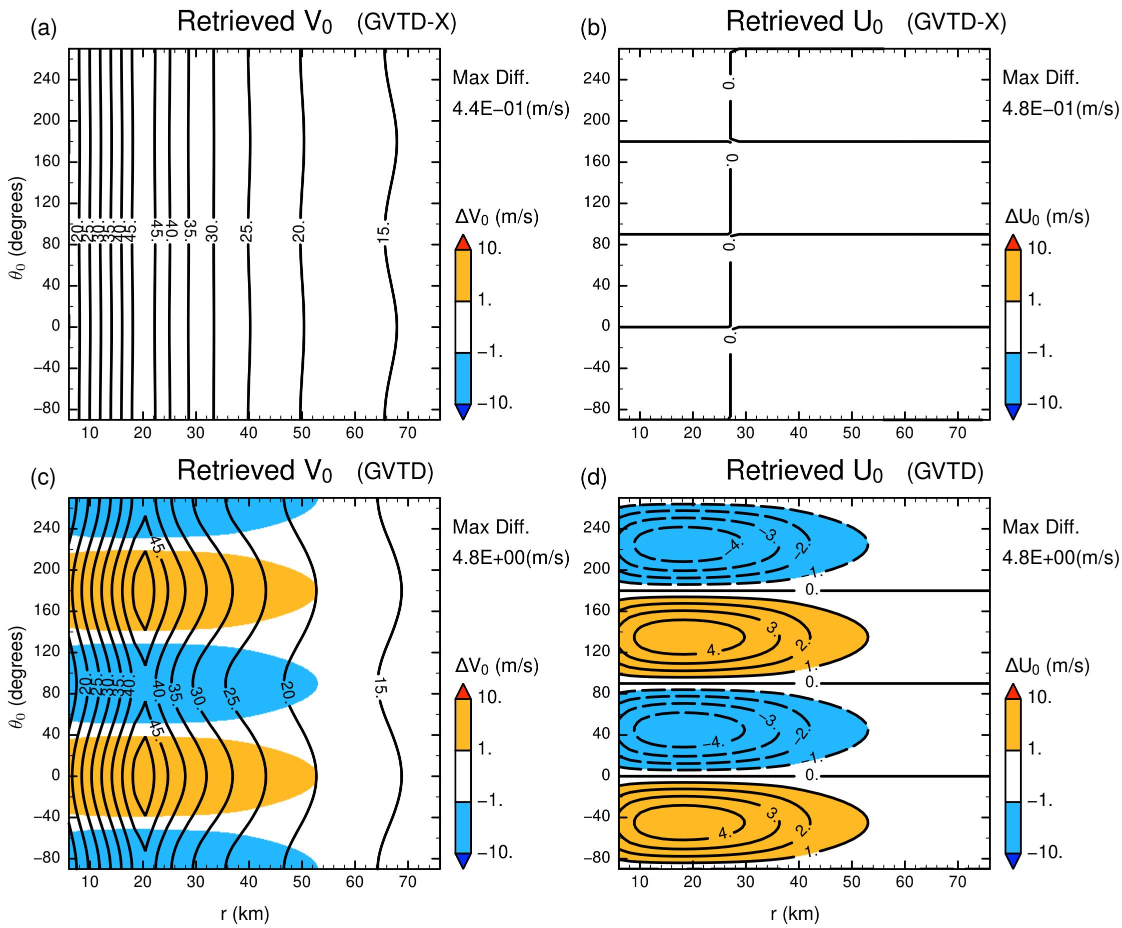

FIG. 5. Radial distributions of the retrieved axisymmetric (left) tangential and (right) radial winds in VRW2-VORTEX for various θ_0 in Eq. (52), indicated by contours. For example, $\theta_0 = 0°$ and 180° are identical to the case of Fig. 4. Top and bottom panels denote the GVTD-X and GVTD retrieval results, respectively. Shading indicates the difference of the axisymmetric winds between the retrieved and true vortices. Contour intervals are every 5 m s^{-1} in the left panels and every 1 m s^{-1} in the right panels.

We further examine the dependence of the azimuthal phase of the wavenumber-2 asymmetric structure on the retrieved axisymmetric circulations (V_0 and U_0). Lee et al. (1999) examined the GBVTD retrieval for the wavenumber-2 vortices with the specific angle of 90°, 135°, and 180° in their Figs. 7 and 14. Following Lee et al. (1999), we continuously changed the azimuthal phase for the wavenumber-2 structure in VRW2-VORTEX by sweeping θ_0 ($-90° \leq \theta_0 \leq 270°$) in Eq. (52). Figure 5 shows the retrieved axisymmetric circulations with continuously changing the azimuthal phase for the wavenumber-2 structure. The differences in the axisymmetric circulations between the GVTD-X retrieval and analysis are less than 1 m s^{-1} at all radii (Figs. 5a and 5b). We focus on the difference in the axisymmetric tangential wind at the RMW of 20 km between the retrieval and analysis. The difference in GVTD-X is much smaller than the difference of about 5 m s^{-1} in GVTD which has strong dependence of the retrieved axisymmetric winds on θ_0 (Figs. 5c and 5d). It indicates that the retrieval of the axisymmetric tangential wind can be improved by including asymmetric radial winds in the closure assumption.

Following J08, we examined the sensitivities of errors in the storm-center estimateon to the retrieval of the axisymmetric tangential and radial winds in AX-VORTEX with the RMW of 30 km. Figure 6 shows the retrieval results in a case of difference in the estimated storm center between the analysis and retrieval. As with GVTD, the tangential wind retrieved from GVTD-X had not only the axisymmetric component but also wavenumber-1 asymmetry. In contrast to GVTD, the GVTD-X retrieval had wavenumber-1 asymmetries of the radial wind (Fig. 6d). If the true storm center is at $(R_T + \Delta x,\ \Delta y)$, winds associated with the storm can be expressed within the RMW as follows:

$$\begin{aligned} u &= -\frac{V_{\max}}{r_{\max}}(y-\Delta y), \\ \upsilon &= \frac{V_{\max}}{r_{\max}}(x-R_T-\Delta x), \quad ((x-R_T-\Delta x)^2+(y-\Delta y)^2)^{1/2} \leq r_{\max}). \end{aligned} \tag{53}$$

From Eq. (53), the radial and tangential winds with respect to the estimated storm center $(R_T, 0)$ are expressed as follows:

$$\begin{aligned} U &= u\cos\theta + \upsilon\sin\theta \\ &= \frac{V_{\max}}{r_{\max}}(\Delta y\cos\theta - \Delta x\sin\theta), \end{aligned} \tag{54}$$

$$\begin{aligned} V &= -u\sin\theta + \upsilon\cos\theta \\ &= V_{\max}\frac{r}{r_{\max}} - \frac{V_{\max}}{r_{\max}}(\Delta y\sin\theta + \Delta x\cos\theta). \end{aligned} \tag{55}$$

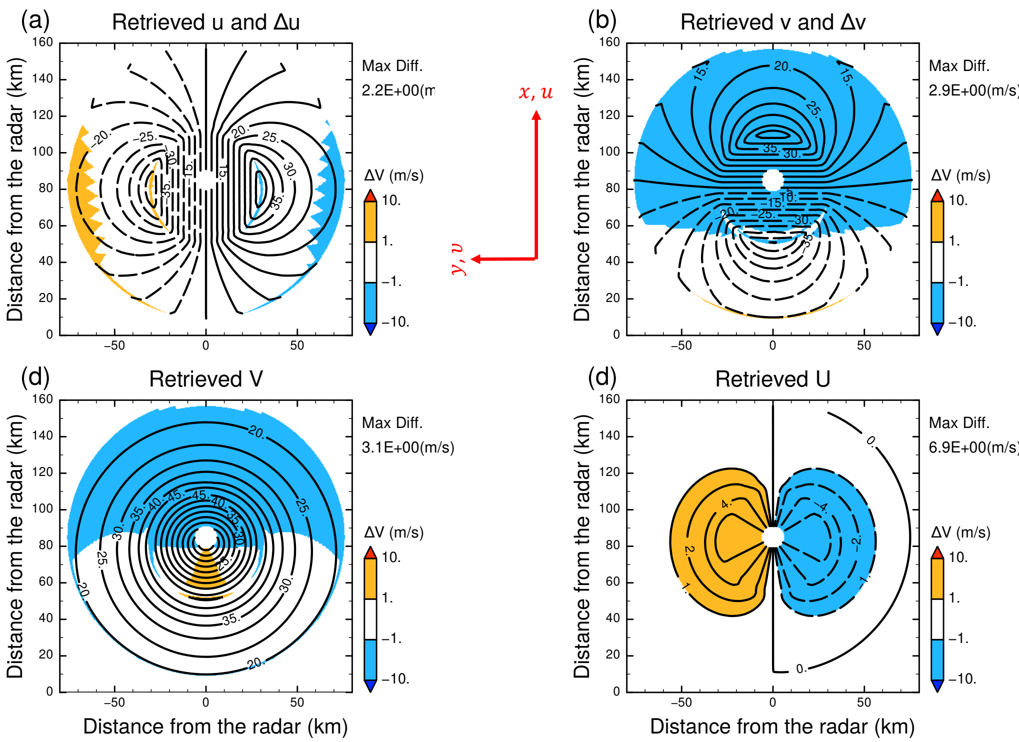

FIG. 6. Horizontal distributions of the (a) x-, (b) y-, (c) tangential, and (d) radial winds retrieved by GVTD-X with an error of the estimated vortex center in AX-VORTEX with the RMW of 30 km. The estimated storm center is located at $R_T = 85$ km from the radar. The true center position has the difference of $\Delta x = -5$ km from the estimated center. Note that the Cartesian coordinates (x, y) follow Fig. 1 as shown in the red vectors. Thus, the true and estimated centers are located at $(R_T + \Delta x, 0)$ and $(R_T, 0)$ on the Cartesian coordinates, respectively. The contour intervals in (a)–(c) and (d) are every 5 m s^{-1} and 1, 2, 4, and 6 m s^{-1}, respectively. The difference from the analytical vortex is shown by the color shade.

Equations (54) and (55) indicate that errors of the storm-center estimation in the retrieval cause spurious signals, which cannot be interpreted as physical phenomena such as wavenumber-1 VRWs, in both wavenumber-1 components of the radial and tangential winds.[2] In fact, the retrieval errors in x- and y-components of the GVTD-X-retrieved winds are less than those in the radial and tangential winds which depend on the storm center (Figs. 6a and 6b).

[2]Equations (54) and (55) also indicate that the spurious signals are amplified as the distance from the true center increases, as shown in J08.

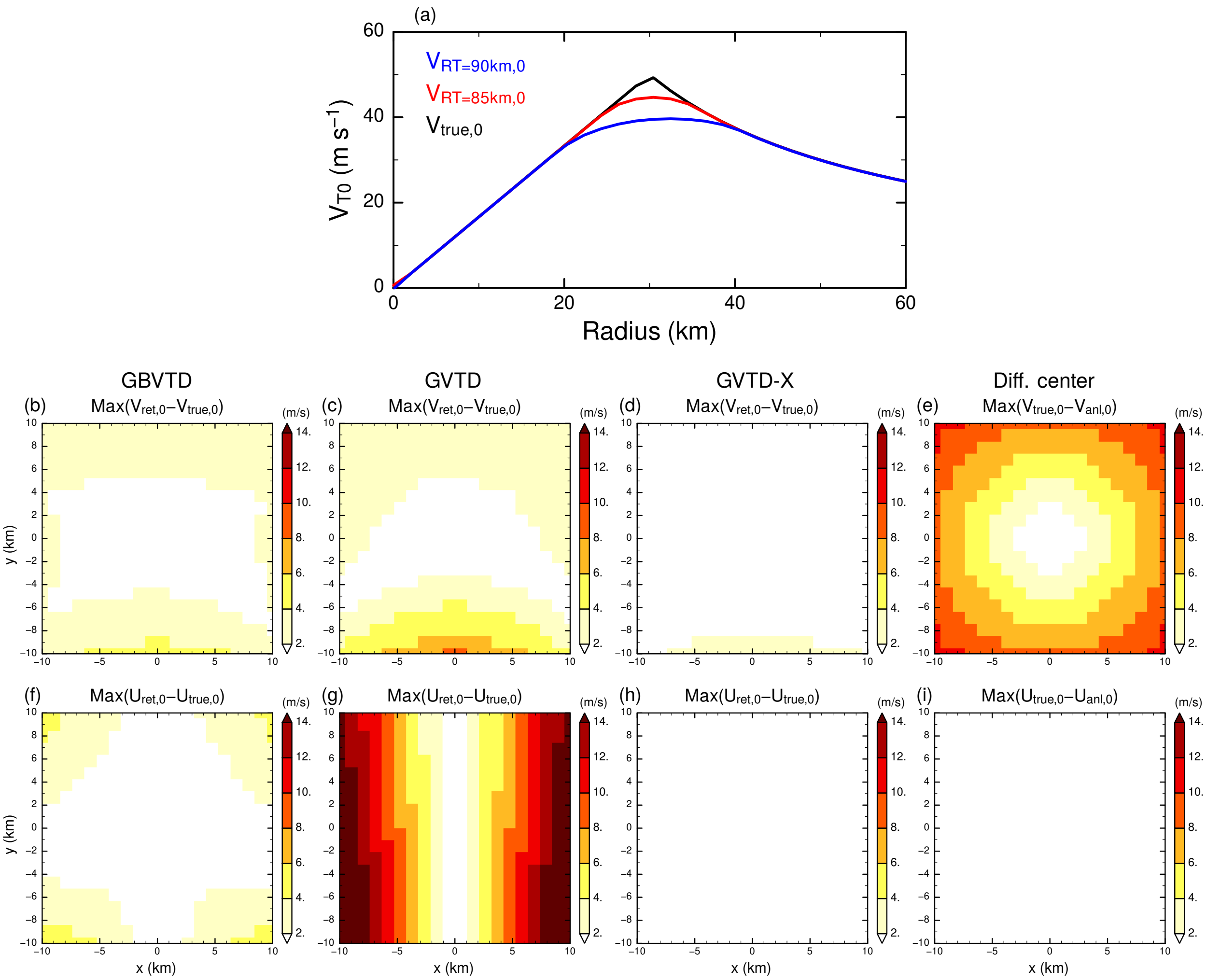

FIG. 7. (a) The axisymmetric tangential wind profiles of AX-VORTEX with respect to (black) the true center located at 80 km from the radar and the misplaced storm centers at (red) $R_T = 85$ km and (blue) $R_T = 90$ km and (b-i) the distributions of the maximum errors of the axisymmetric (middle) tangential and (bottom) radial winds in AX-VORTEX with the RMW of 30 km by (b) and (f) GBVTD, (c) and (g) GVTD, and (d) and (h) GVTD-X retrievals with errors of the storm center estimation. The errors are defined as the differences between the retrieved and analytical winds with respect to each misplaced center. The abscissa and ordinate indicate the distance of the estimated center as a function of x and y from the true center ($x = 80$ km, $y = 0$ km). Panels (e) and (i) indicate the distributions of the maximum differences in the tangential and radial winds of AX-VORTEX with respect to the misplaced and true centers.

We now focus on the axisymmetric components. To distinguish pure retrieval errors in axisymmetric winds from errors by the misplacement of the estimated storm center, we defined the maximum retrieval errors as the maximum differences of the retrieved wavenumber-0 winds from the wavenumber-0 component of AX-VORTEX with respect to the misplaced center. The maximum differences between the winds in AX-VORTEX with respect to the misplaced and true centers are defined as the estimation errors of the storm center (Fig. 7a). Even if we can choose the perfect retrieval method, the retrieved winds have the estimation errors of the storm center (i.e., the maximum difference between the black and red or blue lines in Fig. 7a). Note that the errors by the misplacement were not separated from the retrieval errors in the C-series of J08. Figure 7 shows the dependence of the maximum retrieval errors of axisymmetric tangential and radial winds on the estimation errors of the storm center among GBVTD, GVTD, and GVTD-X. The maximum retrieval errors in the tangential and radial winds between GVTD-X and analysis was mostly less than 2 m s^{-1} within the storm-center misplacement of 10 km (Figs. 7d and 7h). The small retrieval errors for the misplacement were advantages of GVTD-X over GBVTD and GVTD (Figs. 7b, 7c, 7f, and 7g). On the other hand, the axisymmetric tangential wind of the analytical vortex with respect to the misplaced center increased the difference from the prescribed profile of the analytical vortex as the distance from the true center increases, independent on the retrieval methods (the red and blue lines in Fig. 7a or Fig. 7e). The errors for the tangential winds shown in the C-series of J08 mainly corresponds to the estimation errors of the storm center, rather than the retrieval errors. The radial wind has small errors for the misplacement of the estimated storm center (Fig. 7i). Thus, the errors in the GVTD-retrieved radial winds are mainly caused by ignoring the asymmetric radial winds in the closure assumptions.

4. Application to a real observed typhoon

a. Overview

The GVTD-X technique is applied to a real typhoon. The target is Typhoon Haishen (2020), which had CEs in passing over the Okinawa region. After the secondary eyewall formation, the inner eyewall exhibited an elliptical structure, and the elliptical structure had a counterclockwise rotation with a period of about 1 h for wavenumber-2 components (Fig. 8). The deformation of the inner eyewall to the elliptical shape might be due to the barotropic interaction with the outer eyewall (e.g., Kossin et al. 2000; Lai et al. 2019). According to the knowledge from the barotropic

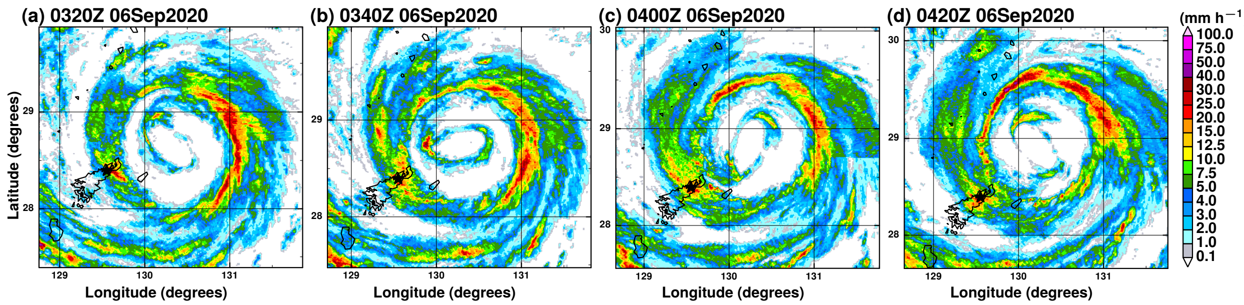

FIG. 8. Elliptical eyewalls in Typhoon Haishen (2020) captured by the JMA C-band operational Doppler radar at Naze (the black stars). The color indicates the precipitation intensity (mm h^{-1}) converted from the radar reflectivity.

TABLE 2. The Doppler velocity data processing.

1.	Dealiasing of the Doppler velocity beyond the Nyquist range (Yamauchi et al. 2006)
2.	Interpolating from PPI to CAPPI (200-km radius and 10-km height from the radar)
3.	Determining TC centers subjectively^{a}
4.	Interpolating the Doppler velocity data from CAPPI to TC cylindrical coordinates

a: Due to the strong asymmetric structure in Haishen, objective methods to determine the TC center, such as the GBVTD-simplex center-finding algorithm (Lee and Marks 2000; Bell and Lee 2012), were not used in the present study.

point of view, it is expected that the asymmetric radial flow will be similar order to the asymmetric tangential flow, coinciding with the wavenumber-2 vorticity in the elliptic eyewall (Lai et al. 2019).

We use the ground-based C-band Doppler radar operated by the Japan Meteorological Agency (JMA), located at Naze on the Amami Oshima island (Fig. 8). Following Shimada et al. (2016), the Doppler velocity data on the TC cylindrical coordinates at a height of 2 km are produced from constant altitude PPI (CAPPI) data (Table 2 and Fig. 9a). The radial and azimuthal grid spacings on the cylindrical coordinates are 2 km and 2.8125° (i.e., 128 samplings), respectively. The retrieval is performed within the innermost and outermost radii with missing less than 64 points along the azimuth. There are few sampling points in the moat of Haishen (Fig. 9a). If data missing along azimuth is greater than 64 at a radius in between the innermost and outermost radii, the radius is not used in retrieval by introducing the unused radius. The retrieved variables are V_0, U_0, $\Phi_{S,k}$, and $\Phi_{C,k}$ ($k \leq 3 = N$). The sensitivity of the use of different maximum wavenumbers to the retrieval is examined in section 4c.

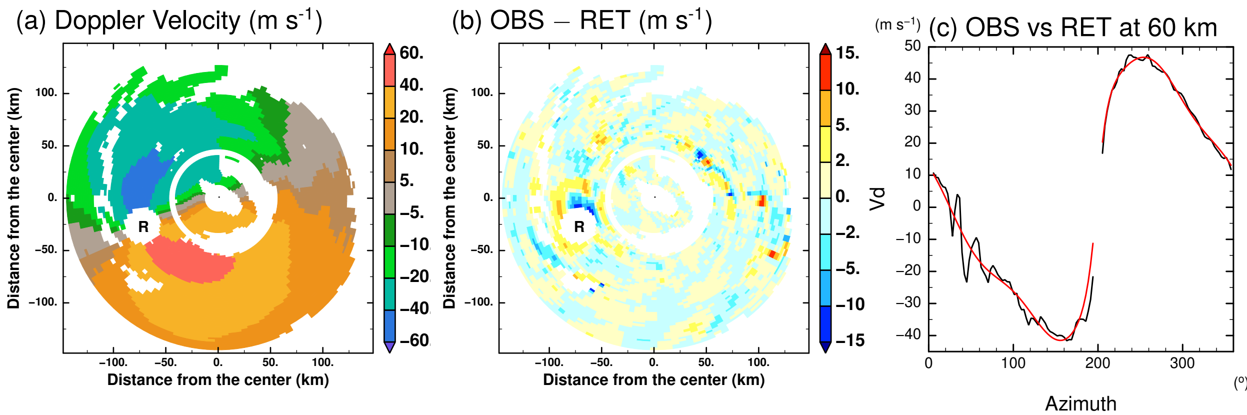

FIG. 9. (a) A snapshot of the Doppler velocity in Typhoon Haishen at the 2-km height, (b) difference in the Doppler velocity between the observation and retrieval in (a), and (c) the Doppler velocities of the (black) observation and (red) retrieval at the radius of 60 km in (a). The snapshot is the time of Fig. 8a. The capital "R" indicates the radar position.

b. Results

Figures 9b and 9c show the difference in the Doppler velocity between the observation and retrieval at a certain time. The difference in the Doppler velocity greater than 10 m s^{-1} is exhibited in the outer eyewall. The difference with the large amplitude is associated with high-wavenumber structures in azimuth, suggesting the difference is mainly due to divergent flows and rotational flows with higher wavenumbers at a convective scale (Fig. 8a). On the other hand, the low-wavenumber feature of the observed Doppler velocity is reasonably captured as shown in Fig. 9c.

Figure 10a shows the time series of the retrieved axisymmetric tangential wind in GVTD-X with the outer constraint for $\Phi_{C,1}$ of no storm-relative mean wind (i.e., $\upsilon_M = \upsilon_S$). The inner eyewall is located within 20- to 40-km radii, and the outer eyewall is beyond the 60-km radius. The maximum of the retrieved axisymmetric tangential wind in the inner (outer) eyewall is more than 40 m s^{-1} (50 m s^{-1}) in the early period of the analysis. The tangential wind maximum in the outer eyewall is maintained in time. On the other hand, the tangential wind in the inner eyewall gradually decreases in time, which might be associated with an eyewall replacement cycle.

We examined the sensitivity of the storm-relative mean wind ($\upsilon_M \neq \upsilon_S$) in the outer constraint for $\Phi_{C,1}$ to the axisymmetric tangential wind retrieval (Fig. 10b). The mean wind υ_M was calculated from the Japanese 55-year Reanalysis (JRA55; Kobayashi et al. 2015). The difference

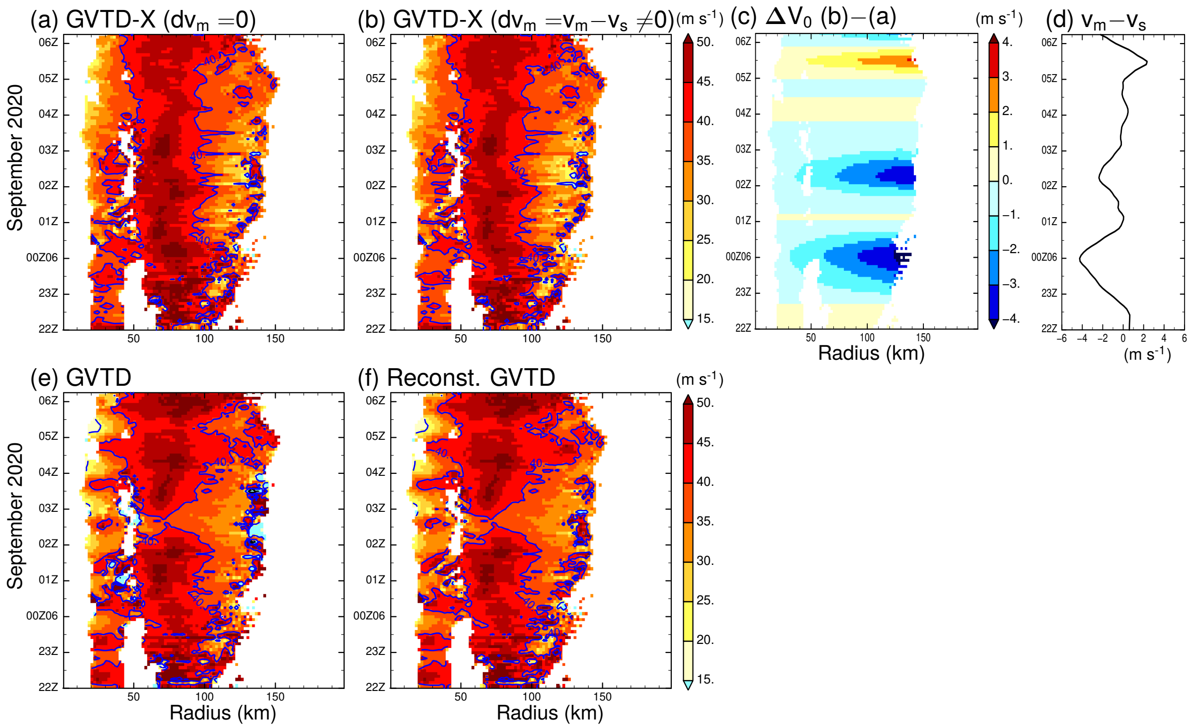

FIG. 10. Radius-time cross-sections of axisymmetric tangential winds (color; m s^{-1}) at the 2-km height retrieved in Haishen based on (a) and (b) GVTD-X, (e) GVTD, and (f) reconstructed-GVTD. The GVTD-X retrievals in (a) and (b) used the outer constraints of $\upsilon_M = \upsilon_S$ and $\upsilon_M (\neq \upsilon_S)$ from the JRA55 dataset for $\Phi_{C,1}$, respectively [Eqs. (46) and (47)]. Panel (c) denotes the difference in the axisymmetric tangential winds between (a) and (b). The evolution of $\upsilon_M - \upsilon_S$ is shown in (d). The reconstructed-GVTD profile is produced by aliasing the asymmetric radial flows retrieved in GVTD-X to the axisymmetric tangential wind, based on Eq. (17) of J08. The blue contours denote the axisymmetric tangential wind of 40 m s^{-1}. In the retrievals of (e) and (f), $\upsilon_M = \upsilon_S$.

in the retrieved tangential winds between the $\upsilon_M \neq \upsilon_S$ and $\upsilon_M = \upsilon_S$ constraints increased with the radius during certain periods (2300 UTC 05-0100 UTC 06, 0200 UTC-0300 UTC 06, and 0500 UTC-0600 UTC 06 September), as shown in Fig. 10c. This feature is quantitatively explained by the dependency of the constraint for $\Phi_{C,1}$ on radius (i.e., $V_0 = \rho^{-1}(\upsilon_M - \upsilon_S)$), as discussed in section 2e (see also Figs. 10d and S1). It indicates that the constraint for $\Phi_{C,1}$ at the outermost radius can influence the retrieval of the axisymmetric tangential wind at other radii. Thus, to assess the accurate storm-relative mean wind is important for the accurate retrieval.

As a reference, we also performed the GVTD retrieval with $\upsilon_M = \upsilon_S$ from the same Doppler velocity data (Fig. 10e). The evolution of the axisymmetric tangential wind in the GVTD retrieval are in good agreement with those in the GVTD-X retrieval. On the other hand, the GVTD-retrieved tangential winds exhibited systematic fluctuation with a period of $\sim$ 1 h at around a 30-km radius in the inner eyewall, synchronized with the counterclockwise rotation of the elliptical shape of the inner eyewall (Fig. 8). The fluctuation of the tangential winds had an amplitude of about 5 m s^{-1}. The fluctuation is the aliasing (i.e., spurious signal) of the asymmetric radial flows to the axisymmetric tangential wind due to the closure in GBVTD and GVTD, as pointed out by Lee et al. (1999) and shown in Fig. 5c. It is also shown from the fact that the GVTD-retrieved winds can be reconstructed by the GVTD-X-retrieved $V_0 - U_{S,2} - (U_{S,1} + U_{S,3})\rho^{-1}$, based on Eq. (17) of J08[3] (Figs. 10e and 10f). The new closure including asymmetric radial flows can eliminate the aliasing, and retrieve the axisymmetric tangential winds even in cases of asymmetric vortices.

Figure 11 shows the wavenumber-2 winds in GVTD-X. The wavenumber-2 winds in the inner eyewall had a confluent-difluent flow pattern. From the phase relation between U and Φ or vorticity, they are out of phase by $\pi/2$. In fact, the inflows and outflows for the wavenumber 2 are not located on the major and minor axes of the ellipse of the inner eyewall, which is consistent with a numerical simulation (Figs. 3 and 4 in Lai et al. 2019). It indicates that GVTD-X can retrieve consistently asymmetric flows by including the radial components.

c. Error evaluation from the consistency by changing N

So far, we have left the choice of maximum wavenumber N arbitrary in GVTD-X. Considering the aliasing in the discrete Fourier transform, Lee et al. (2000) proposed to set the maximum wavenumber at each radius from the longest contiguous data gap along azimuth. However, unlike GBVTD or GVTD, all radii are combined in GVTD-X, so the same approach is not necessarily fruitful. Here we examine the consistency of the retrieval by varying N. Such examination can be used not only to set N but also to estimate retrieval errors, which was unavailable with GBVTD or GVTD.

Figure 12a shows the axisymmetric tangential winds by considering the storm-relative mean wind ($\upsilon_M \neq \upsilon_S$) as in Fig. 10b but for averaging the results with N = 2, 3, and 4. We examine consistency across N by using the coefficient of variation (CV), which is defined as the standard

---

[3] Eq. (17) in J08 is easily rearranged:

$$V_0 - U_{S,2} - \rho^{-1}\left(U_{S,1} + U_{S,3}\right) = -B_1 - B_3 - \rho^{-1}\upsilon_M.$$

The left-hand side is identical to the GVTD-retrieved axisymmetric tangential wind because of $U_{S,2} = U_{S,1} = U_{S,3} = 0$. Thus, we can reconstruct the GVTD-retrieved axisymmetric tangential wind by the GVTD-X-retrieved $V_0 - U_{S,2} - (U_{S,1} + U_{S,3})\rho^{-1}$.

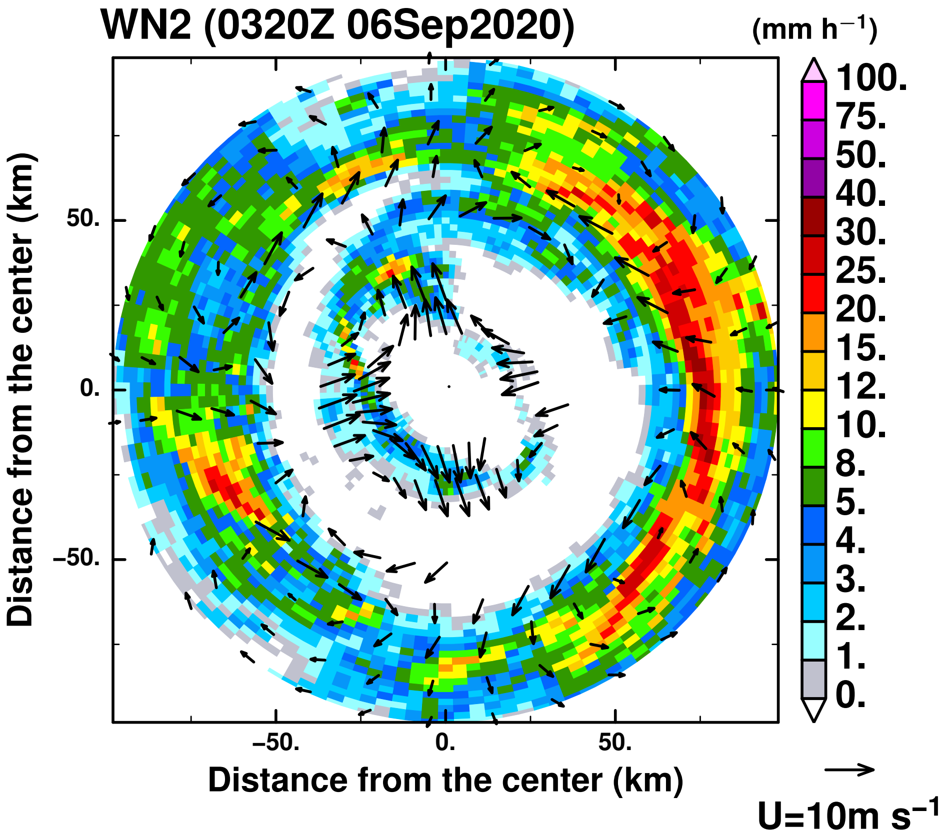

FIG. 11. As in Fig. 8a, except for superposing the wavenumber-2 components of the GVTD-X-retrieved rotating winds by arrows at 0320 UTC on 06 September 2020.

deviation divided by the mean over the N values (Fig. 12b). High CVs (> 10%) are exhibited near the moat (at around 0100 UTC 06 September 2020, particularly) and the outermost radii. The areas with the high CV values correspond to radii with relatively fewer sampling numbers (Fig. 12c). Figure 13a shows the frequency distribution of the CV in terms of sampling gaps. As the percentage of the sampling number increases, the CV tends to decrease. Particularly, when the percentage of the sampling number is greater than 75% of the whole azimuthal angle at a radius, small CV values (< 10%) are mostly exhibited in the retrievals among the three cases. The assessment clarifies that the retrieved axisymmetric tangential winds with the maximum wavenumber of 3 (Fig. 10b) is robust, except for the radii with a relatively less percentage of the sampling number (< 75%) near the moat and outer boundary (Fig. 12c). As a reference, the frequency distribution of the CV in the largest single data gap based on Lee et al. (2000) is also shown Fig. 13b. As with Fig. 13a,

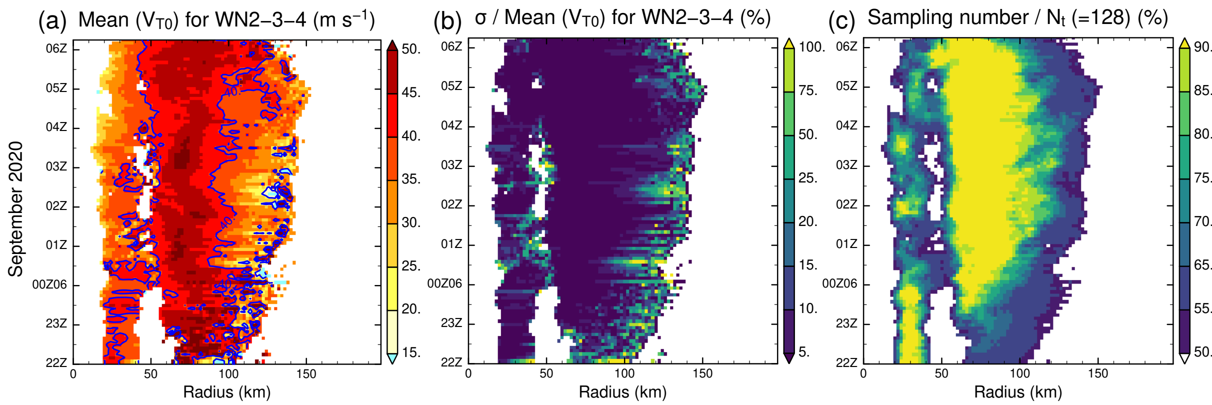

FIG. 12. Radius-time cross-sections of (a) the average and (b) the coefficient of variation for the axisymmetric tangential winds retrieved among the three cases with different maximum wavenumbers of 2, 3, and 4 at the 2-km height. As in Fig. 10b, the outer constraint of $\upsilon_M \neq \upsilon_S$ for $\Phi_{C,1}$ is given in the three cases. Panel (c) denotes the percentage of the azimuthal sampling number at each radius and time.

small CV values (< 10%) concentrate on small data gaps (< 90°). The concept of the largest single data gap might be still useful for the assessment of the robust retrieval in the new method which requires the radial continuity of the asymmetric streamfunctions.

The statistical features (mean, standard deviation, and CV) in the retrievals with different maximum wavenumbers can be used as a guideline for the robust retrieval of the axisymmetric tangential winds in GVTD-X. For example, we can trust the retrieval near the storm center with low standard deviations, compared with that near the moat and outermost radii with high standard deviations due to less sampling number in Haishen. The decrease in the axisymmetric tangential wind within a 40-km radius (i.e., in the inner eyewall) can be an actual vortex evolution, associated with the inner eyewall decay (Fig. 14). Note that the statistical features do not indicate errors from truth. In retrieving the axisymmetric winds, we can use the mean and standard deviation over different N, instead of the retrievals from a single N. Although the statistical features over N =2, 3, and 4 were used in the present study, a set of the maximum wavenumbers is changeable. Moreover, we can determine the most representative N by examining the standard deviation for each case.

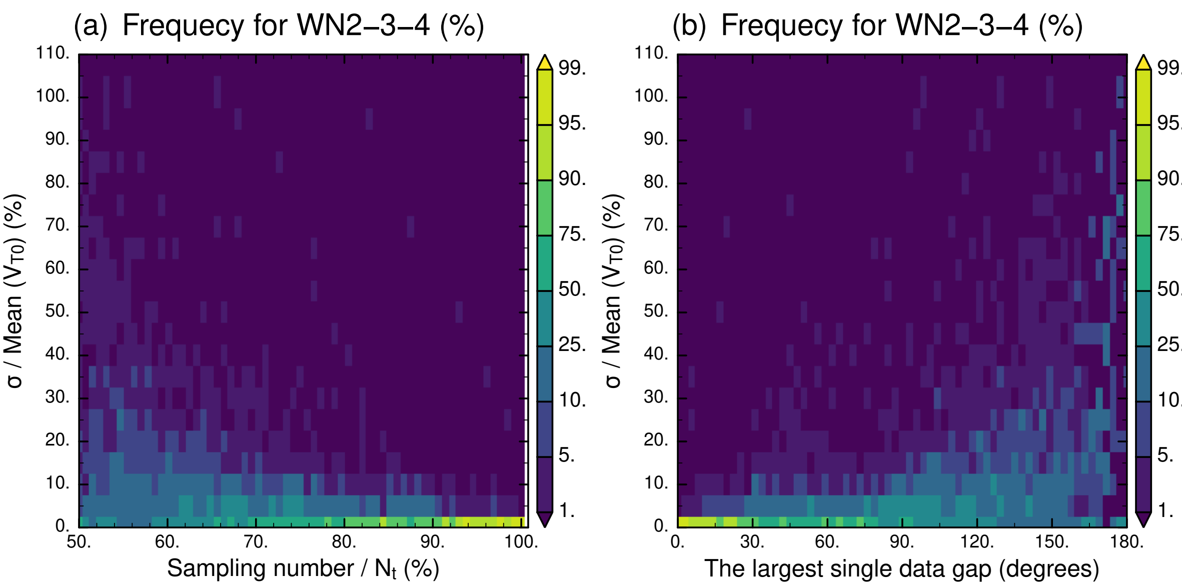

FIG. 13. The frequency distribution (color; %) of the coefficient of variation for the retrieved axisymmetric tangential winds among the three cases in each (a) sampling number (the percentage for the total number of the sampling $N_t = 128$ at a radius) and (b) largest single data gap. The coefficient of variation is calculated by the retrieval results at all radii and times in Fig. 12.

5. Concluding remarks

GBVTD and GVTD assumed the closure of no asymmetric radial flows in the retrieval formula. In the present study, we proposed a new closure assumption and retrieval formulas in GVTD, being allowed to include asymmetric radial flows, named as GVTD-X. Based on the Helmholtz decomposition theorem, streamfunction and velocity potential are used in the retrieval, in contrast to asymmetric winds in GVTD. The asymmetric radial winds are represented by the azimuthal gradient of the retrieved asymmetric streamfunctions. Another novelty is that, unlike GBVTD and GVTD that solve equations independently at each radius, GVTD-X uses simultaneous equations to solve for the entire radial grid points at once. The simultaneous solution introduces consistency along radius. We proposed a guideline for an error estimation of the retrieval by statistical features (i.e., mean, standard deviation, and coefficient of variation) over the GVTD-X-retrieved axisymmetric tangential winds with different maximum wavenumbers.

The GVTD-X retrieval was applied to analytical vortices. In the case of the Rankine vortex with wavenumber-2 VRWs, the difference in the tangential winds between the analytical and retrieved

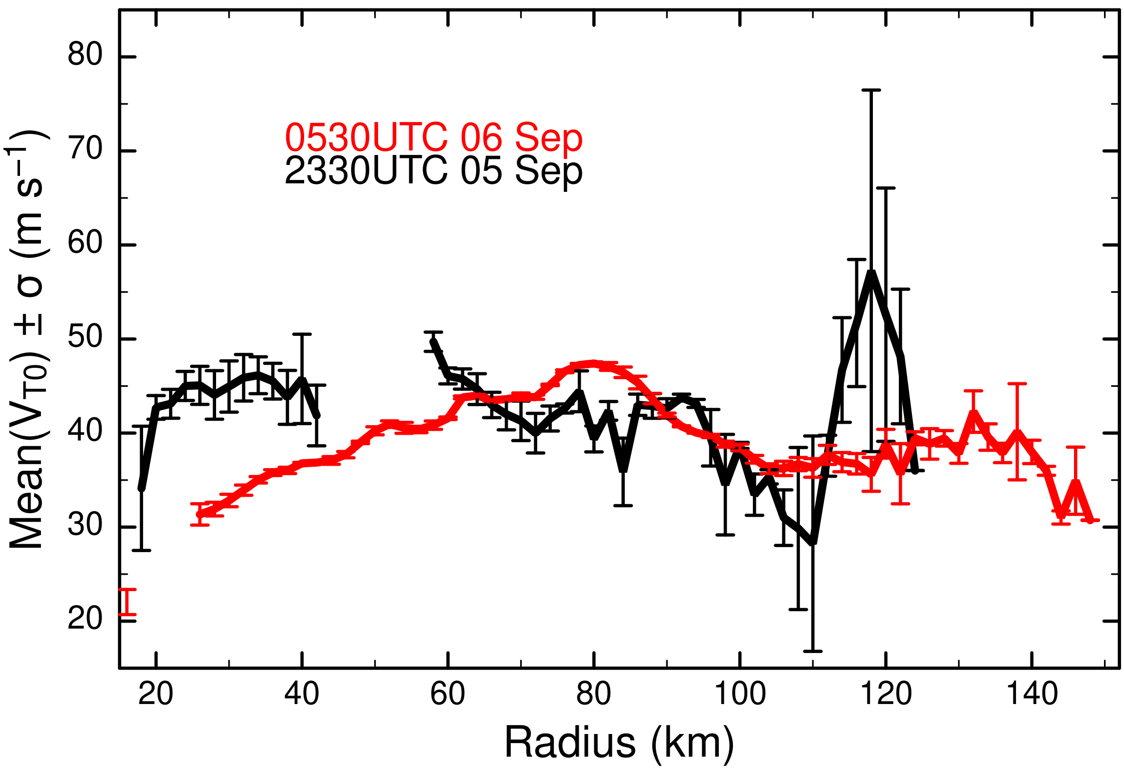

FIG. 14. Radial distributions of the mean and standard deviation of the GVTD-X-retrieved axisymmetric tangential winds over $N = 2$, 3, and 4. The whisker plot indicates the standard deviation.

vortices was less than 1 m s^{-1} near the RMW (the relative error of $\leq 2\%$). On the other hand, errors of the retrieved tangential winds increased near the outermost radius of the retrieval area because of additional constraints required for the asymmetric streamfunctions at the outermost radius in the retrieval. The sensitivity of the GVTD-X retrieval to the misplacement of the estimated storm center was compared with those in GBVTD and GVTD. The GVTD-X retrieval errors of the axisymmetric tangential and radial winds are the smallest of the three methods, which is an advantage over the other methods.

The GVTD-X technique was applied to the axisymmetric tangential winds in concentric eyewalls with an elliptical shape of Typhoon Haishen (2020) observed by a ground-based Doppler radar. GVTD-X estimated the axisymmetric tangential wind of about 40 m s^{-1} in the inner eyewall. The estimated tangential wind gradually decreased. The GVTD-X retrieval was qualitatively consistent with that in GVTD. However, the GVTD-retrieved axisymmetric tangential winds exhibited the fluctuation with the period of 1 h in the inner eyewall, which was synchronized with the counterclockwise rotation of the elliptical shape of the inner eyewall. The fluctuation in GVTD was mostly reduced by the GVTD-X retrievals. We concluded that the systematic fluctuation was a spurious signal mainly due to the closure assumption of GVTD. Note that the GVTD-X-retrieved axisymmetric tangential winds also depend on the storm-relative mean wind even in following the guideline based on the statistical features, so the accurate estimation of the mean wind is also required.

In the future, the validity of GVTD-X should be investigated by the application to various typhoons. Moreover, we should assess the accuracy of the GVTD-X retrieval by comparison with full-physics numerical model results (Shimada et al. 2016) or other observations such as dual Doppler analysis (Cha and Bell 2021). Finally, GVTD-X can retrieve asymmetric vorticity fields associated with vortices. Thus, the new technique can be useful for evaluating theoretical and modelling studies of internal dynamics such as VRWs, which has been developed on barotropic frameworks (e.g., Montgomery and Kallenbach 1997; Schubert et al. 1999; Kossin et al. 2000; Kossin and Schubert 2001; Lai et al. 2019).

Acknowledgments. This study used the DCL of the GFD-Dennou-Club (http://www.gfd-dennou.org/library/dcl/) drawing library. This work was supported by a Japan Society for the Promotion of Science (KAKENHI) grant numbers JP19H00705 and JP21H04992.

Data availability statement. The codes for GVTD-X are available from https://github.com/tomonori-93/GVTD-X (Tsujino 2023). The JMA Doppler radar data are available through the Japan Meteorological Business Support Center (JMBSC) and the Meteorological Research Consortium, a framework for research cooperation of the JMA and the Meteorological Society of Japan. The JRA-55 data are available from https://rda.ucar.edu/datasets/ds628.0/.

APPENDIX A

Constraint for the velocity potential

To include the non-rotating and non-divergent winds in asymmetric streamfunctions, the asymmetric velocity potential Ψ is constrained by divergence D:

$$\left[\frac{\partial^2}{\partial r^2}+\frac{1}{r}\frac{\partial}{\partial r}+\frac{\partial^2}{r^2\partial\theta^2}\right]\Psi_k(r,\theta)=D_k(r,\theta). \tag{A1}$$

For the Fourier components (Ψ_k and D_k) for the wavenumber$-k$,

$$\begin{aligned}\Psi_k(r,\theta)&=\Psi_{S,k}(r)\sin(k\theta)+\Psi_{C,k}(r)\cos(k\theta),\\ D_k(r,\theta)&=D_{S,k}(r)\sin(k\theta)+D_{C,k}(r)\cos(k\theta),\end{aligned} \tag{A2}$$

Equation (A1) in the wavenumber$-k$ is reduced to the radial structure equations:

$$\left[\frac{\partial^2}{\partial r^2}+\frac{1}{r}\frac{\partial}{\partial r}-\frac{k^2}{r^2}\right]\left[\begin{array}{c}\Psi_{S,k}\\ \Psi_{C,k}\end{array}\right]=\left[\begin{array}{c}D_{S,k}\\ D_{C,k}\end{array}\right],\quad (k\in\mathbb{N}). \tag{A3}$$

The impulse response of a source at r' in Eq. (A3) can be expressed by the Green function in Eq. (28). Thus, the solutions of Eq. (A3) can be expressed as superposition of G_k and $D_{S,k}$ or $D_{C,k}$:

$$\left[\begin{array}{c}\Psi_{S,k}(r)\\ \Psi_{C,k}(r)\end{array}\right]=\int_0^\infty r'G_k(r;r')\left[\begin{array}{c}D_{S,k}(r')\\ D_{C,k}(r')\end{array}\right]dr', \tag{A4}$$

Thus, Ψ_k in Eq. (A2) can be expressed by Eq. (A4):

$$\Psi_k(r,\ \theta) = \int_0^\infty r' G_k(r;r') D_{S,k}(r') dr' \sin(k\theta) + \int_0^\infty r' G_k(r;r') D_{C,k}(r') dr' \cos(k\theta). \qquad \text{(A5)}$$

APPENDIX B

Degree of freedom in Equation (30)

If we suppose $L \leq N$ in Eq. (20), the Fourier expansions of U and V can be written as

$$\begin{aligned} U &= \sum_{k=1}^{N} U_{S,k} \sin(k\theta) + \sum_{k=0}^{N} U_{C,k} \cos(k\theta), \\ V &= \sum_{k=1}^{N} V_{S,k} \sin(k\theta) + \sum_{k=0}^{N} V_{C,k} \cos(k\theta), \end{aligned} \qquad \text{(B1)}$$

In substituting Eq. (B1) into Eq. (13),

$$\begin{aligned} \mathcal{V}_d'\delta = &\sum_{k=1}^{N} \left[U_{S,k} \sin(k\theta) + \rho U_{S,k} \sin(k\theta)\cos\theta - \rho V_{S,k} \sin(k\theta)\sin\theta \right] \\ &+ \sum_{k=0}^{N} \left[U_{C,k} \cos(k\theta) + \rho U_{C,k} \cos(k\theta)\cos\theta - \rho V_{C,k} \cos(k\theta)\sin\theta \right]. \end{aligned} \qquad \text{(B2)}$$

From the following trigonometric identities:

$$\begin{aligned} \sin(k\theta)\cos\theta &= \frac{1}{2}\left[\sin(k+1)\theta + \sin(k-1)\theta\right], \\ \sin(k\theta)\sin\theta &= \frac{1}{2}\left[-\cos(k+1)\theta + \cos(k-1)\theta\right], \\ \cos(k\theta)\cos\theta &= \frac{1}{2}\left[\cos(k+1)\theta + \cos(k-1)\theta\right], \\ \cos(k\theta)\sin\theta &= \frac{1}{2}\left[\sin(k+1)\theta - \sin(k-1)\theta\right], \end{aligned}$$

Equation (B2) can be expressed as follows:

$$
\begin{aligned}
\mathcal{V}_d'\delta = {} & U_{C,0} + \frac{\rho}{2}\left(U_{C,1} - V_{S,1}\right) \\
& + \left[U_{C,1} + \frac{\rho}{2}\left(-V_{S,2} + 2U_{C,0} + U_{C,2}\right)\right]\cos\theta \\
& + \left[U_{S,1} + \frac{\rho}{2}\left(U_{S,2} - 2V_{C,0} + V_{C,2}\right)\right]\sin\theta \\
& + \sum_{k=2}^{N-1}\left\{\left[U_{C,k} + \frac{\rho}{2}\left(V_{S,k-1} - V_{S,k+1} + U_{C,k-1} + U_{C,k+1}\right)\right]\cos\left(k\theta\right)\right\} \\
& + \sum_{k=2}^{N-1}\left\{\left[U_{S,k} + \frac{\rho}{2}\left(U_{S,k-1} + U_{S,k+1} - V_{C,k-1} + V_{C,k+1}\right)\right]\sin\left(k\theta\right)\right\} \\
& + \left[U_{C,N} + \frac{\rho}{2}\left(V_{S,N-1} + U_{C,N-1}\right)\right]\cos\left(N\theta\right) \\
& + \left[U_{S,N} + \frac{\rho}{2}\left(U_{S,N-1} - V_{C,N-1}\right)\right]\sin\left(N\theta\right) \\
& + \frac{\rho}{2}\left(V_{S,N} + U_{C,N}\right)\cos\left(N+1\right)\theta \\
& + \frac{\rho}{2}\left(U_{S,N} - V_{C,N}\right)\sin\left(N+1\right)\theta.
\end{aligned}
\tag{B3}
$$

Equation (B3) indicates that the retrieved $\mathcal{V}_d'\delta$ is expressed by the Fourier series on the right-hand-side up to wavenumber $N+1$. There, each Fourier coefficient consists of multiple Fourier coefficients of U and V. While the number of the Fourier coefficients in Eq. (B3) is $2N+3$, the total number of the Fourier coefficients of the two wind components in Eq. (B1) is $4N+2$. Since the latter is greater, it is possible that non-zero wind can have no projection on $\mathcal{V}_d'\delta$. From Eq.

(B3),

$$
\begin{aligned}
(k=0) &: U_{C,0}+\frac{\rho}{2}\left(U_{C,1}-V_{S,1}\right)=0,\\
(k=1) &: U_{C,1}+\frac{\rho}{2}\left(-V_{S,2}+U_{C,0}+U_{C,0}+U_{C,2}\right)=0,\\
(k=1) &: U_{S,1}+\frac{\rho}{2}\left(U_{S,2}-V_{C,0}-V_{C,0}+V_{C,2}\right)=0,\\
(2\le k\le N-1) &: U_{C,k}+\frac{\rho}{2}\left(V_{S,k-1}-V_{S,k+1}+U_{C,k-1}+U_{C,k+1}\right)=0,\\
(2\le k\le N-1) &: U_{S,k}+\frac{\rho}{2}\left(U_{S,k-1}+U_{S,k+1}-V_{C,k-1}+V_{C,k+1}\right)=0,\\
(k=N) &: U_{C,N}+\frac{\rho}{2}\left(V_{S,N-1}+U_{C,N-1}\right)=0,\\
(k=N) &: U_{S,N}+\frac{\rho}{2}\left(U_{S,N-1}-V_{C,N-1}\right)=0,\\
(k=N+1) &: V_{S,N}+U_{C,N}=0,\\
(k=N+1) &: U_{S,N}-V_{C,N}=0.
\end{aligned}
\tag{B4}
$$

The non-trivial solution of Eq. (B4) is the source of the ambiguity, which necessitates a closure as in GVTD (J08). The wind components of $U_{C,k}$, $U_{S,k}$, $V_{C,k}$, and $V_{S,k}$ are expressed by the Φ and Ψ from Eqs. (15)–(20):

$$
\begin{aligned}
U_{C,0} &= -\frac{\partial\Psi_0}{\partial r}=U_0,\\
U_{C,k} &= \left[\frac{k}{r}\Phi_{S,k}-\frac{\partial\Psi_{C,k}}{\partial r}\right],\\
U_{S,k} &= -\left[\frac{\partial\Psi_{S,k}}{\partial r}+\frac{k}{r}\Phi_{C,k}\right],\\
V_{C,0} &= -\frac{\partial\Phi_0}{\partial r}=V_0,\\
V_{C,k} &= -\left[\frac{\partial\Phi_{C,k}}{\partial r}+\frac{k}{r}\Psi_{S,k}\right],\\
V_{S,k} &= \left[\frac{k}{r}\Psi_{C,k}-\frac{\partial\Phi_{S,k}}{\partial r}\right].
\end{aligned}
\tag{B5}
$$

Using Eq. (B5), Eq. (B4) can be expressed as follows:

$$(k=0)\ :\ -\frac{\partial \Psi_0}{\partial r}+\frac{\rho}{2}\left(\frac{1}{r}\Phi_{S,1}-\frac{\partial \Psi_{C,1}}{\partial r}-\frac{1}{r}\Psi_{C,1}+\frac{\partial \Phi_{S,1}}{\partial r}\right)=0, \tag{B6}$$

$$(k=1)\ :\ \frac{1}{r}\Phi_{S,1}-\frac{\partial \Psi_{C,1}}{\partial r}-\rho\frac{\partial \Psi_0}{\partial r}+\frac{\rho}{2}\left(-\frac{2}{r}\Psi_{C,2}+\frac{\partial \Phi_{S,2}}{\partial r}+\frac{2}{r}\Phi_{S,2}-\frac{\partial \Psi_{C,2}}{\partial r}\right)=0, \tag{B7}$$

$$(k=1)\ :\ -\frac{\partial \Psi_{S,1}}{\partial r}-\frac{1}{r}\Phi_{C,1}+\rho\frac{\partial \Phi_0}{\partial r}+\frac{\rho}{2}\left(-\frac{\partial \Psi_{S,2}}{\partial r}-\frac{2}{r}\Phi_{C,2}-\frac{\partial \Phi_{C,2}}{\partial r}-\frac{2}{r}\Psi_{S,2}\right)=0, \tag{B8}$$

$$\begin{aligned}(2\le k\le N-1)\ :\ &\frac{k}{r}\Phi_{S,k}-\frac{\partial \Psi_{C,k}}{\partial r}+\frac{\rho}{2}\left(\frac{k-1}{r}\Psi_{C,k-1}-\frac{\partial \Phi_{S,k-1}}{\partial r}+\frac{k-1}{r}\Phi_{S,k-1}-\frac{\partial \Psi_{C,k-1}}{\partial r}\right)\\ &-\frac{\rho}{2}\left(\frac{k+1}{r}\Psi_{C,k+1}-\frac{\partial \Phi_{S,k+1}}{\partial r}-\frac{k+1}{r}\Phi_{S,k+1}+\frac{\partial \Psi_{C,k+1}}{\partial r}\right)=0,\end{aligned} \tag{B9}$$

$$\begin{aligned}(2\le k\le N-1)\ :\ &-\frac{\partial \Psi_{S,k}}{\partial r}-\frac{k}{r}\Phi_{C,k}+\frac{\rho}{2}\left(-\frac{\partial \Psi_{S,k-1}}{\partial r}-\frac{k-1}{r}\Phi_{C,k-1}+\frac{\partial \Phi_{C,k-1}}{\partial r}+\frac{k-1}{r}\Psi_{S,k-1}\right)\\ &-\frac{\rho}{2}\left(\frac{\partial \Psi_{S,k+1}}{\partial r}+\frac{k+1}{r}\Phi_{C,k+1}+\frac{\partial \Phi_{C,k+1}}{\partial r}+\frac{k+1}{r}\Psi_{S,k+1}\right)=0,\end{aligned} \tag{B10}$$

$$\begin{aligned}(k=N)\ :\ &\frac{N}{r}\Phi_{S,N}-\frac{\partial \Psi_{C,N}}{\partial r}\\ &+\frac{\rho}{2}\left(\frac{N-1}{r}\Psi_{C,N-1}-\frac{\partial \Phi_{S,N-1}}{\partial r}+\frac{N-1}{r}\Phi_{S,N-1}-\frac{\partial \Psi_{C,N-1}}{\partial r}\right)=0,\end{aligned} \tag{B11}$$

$$\begin{aligned}(k=N)\ :\ &-\frac{\partial \Psi_{S,N}}{\partial r}-\frac{N}{r}\Phi_{C,N}\\ &-\frac{\rho}{2}\left(\frac{\partial \Psi_{S,N-1}}{\partial r}+\frac{N-1}{r}\Phi_{C,N-1}-\frac{\partial \Phi_{C,N-1}}{\partial r}-\frac{N-1}{r}\Psi_{S,N-1}\right)=0,\end{aligned} \tag{B12}$$

$$(k=N+1)\ :\ \frac{N}{r}\Psi_{C,N}-\frac{\partial \Phi_{S,N}}{\partial r}+\frac{N}{r}\Phi_{S,N}-\frac{\partial \Psi_{C,N}}{\partial r}=0, \tag{B13}$$

$$(k=N+1)\ :\ -\frac{\partial \Psi_{S,N}}{\partial r}-\frac{N}{r}\Phi_{C,N}+\frac{\partial \Phi_{C,N}}{\partial r}+\frac{N}{r}\Psi_{S,N}=0. \tag{B14}$$

Equations (B6)-(B14) can be separated into two independent sets: set A consisting of $\Phi_{S,i}$ and $\Psi_{C,j}$ (i and j are arbitrary integers) as in Eq. (B9), and set B consisting of $\Phi_{C,i}$ and $\Psi_{S,i}$ as in Eq. (B10), if Φ_0 and Ψ_0 are renamed as $\Phi_{C,0}$ and $\Psi_{C,0}$, respectively. It indicates that a mis-evaluation of $\Phi_{S,i}$, for example, can affect Φ_S and Ψ_C at different wavenumbers, but it does not affect Φ_C and Ψ_S. We examine the specific structures of Φ and Ψ leading to ambiguity. The total number of equations in Eqs. (B6)-(B14), E, is $2N+3$, and the number of variables (Φ_0, $\Phi_{C,1}$, $\cdots,\Phi_{S,N}$, Ψ_0, $\Psi_{C,1},\cdots,\Psi_{S,L}$), F, is $2N+2L+2$. Therefore, Eq. (36) is unsolvable if $F>E$. Even though, the nominal number of equations in Eq. (30) can be increased by increasing the number of azimuthal grid points, it does not help because Eqs. (B6)-(B14) holds at the infinite resolution. To close the problem, L needs to be either 0 ($F = E - 1$) or L is 1 but one of $\Psi_{C,1}$ or $\Psi_{S,1}$ is set to zero ($F = E$).

APPENDIX C

Non-trivial solution of the homogeneous equation of Eq. (30) and interdependence among different wavenumbers

According to Appendix B, Eqs. (B6)−(B14) can be reduced:

$$(k=0)\ :\ -\frac{\partial\Psi_0}{\partial r}+\frac{\rho}{2}\left(\frac{1}{r}\Phi_{S,1}-\frac{\partial\Psi_{C,1}}{\partial r}-\frac{1}{r}\Psi_{C,1}+\frac{\partial\Phi_{S,1}}{\partial r}\right)=0, \tag{C1}$$

$$(k=1)\ :\ \frac{1}{r}\Phi_{S,1}-\frac{\partial\Psi_{C,1}}{\partial r}-\rho\frac{\partial\Psi_0}{\partial r}+\frac{\rho}{2}\left(+\frac{\partial\Phi_{S,2}}{\partial r}+\frac{2}{r}\Phi_{S,2}\right)=0, \tag{C2}$$

$$(k=1)\ :\ -\frac{\partial\Psi_{S,1}}{\partial r}-\frac{1}{r}\Phi_{C,1}+\rho\frac{\partial\Phi_0}{\partial r}+\frac{\rho}{2}\left(-\frac{2}{r}\Phi_{C,2}-\frac{\partial\Phi_{C,2}}{\partial r}\right)=0, \tag{C3}$$

$$\begin{aligned}(k=2)\ :\ &\frac{2}{r}\Phi_{S,2}+\frac{\rho}{2}\left(\frac{1}{r}\Psi_{C,1}-\frac{\partial\Phi_{S,1}}{\partial r}+\frac{1}{r}\Phi_{S,1}-\frac{\partial\Psi_{C,1}}{\partial r}\right)\\ &-\frac{\rho}{2}\left(-\frac{\partial\Phi_{S,3}}{\partial r}-\frac{3}{r}\Phi_{S,3}\right)=0,\end{aligned} \tag{C4}$$

$$\begin{aligned}(k=2)\ :\ &-\frac{2}{r}\Phi_{C,2}+\frac{\rho}{2}\left(-\frac{\partial\Psi_{S,1}}{\partial r}-\frac{1}{r}\Phi_{C,1}+\frac{\partial\Phi_{C,1}}{\partial r}+\frac{1}{r}\Psi_{S,1}\right)\\ &-\frac{\rho}{2}\left(\frac{3}{r}\Phi_{C,3}+\frac{\partial\Phi_{C,3}}{\partial r}\right)=0,\end{aligned} \tag{C5}$$

$$\begin{aligned}(3\le k\le N-1)\ :\ &\frac{k}{r}\Phi_{S,k}+\frac{\rho}{2}\left(-\frac{\partial\Phi_{S,k-1}}{\partial r}+\frac{k-1}{r}\Phi_{S,k-1}\right)\\ &-\frac{\rho}{2}\left(-\frac{\partial\Phi_{S,k+1}}{\partial r}-\frac{k+1}{r}\Phi_{S,k+1}\right)=0,\end{aligned} \tag{C6}$$

$$\begin{aligned}(3\le k\le N-1)\ :\ &-\frac{k}{r}\Phi_{C,k}+\frac{\rho}{2}\left(-\frac{k-1}{r}\Phi_{C,k-1}+\frac{\partial\Phi_{C,k-1}}{\partial r}\right)\\ &-\frac{\rho}{2}\left(\frac{k+1}{r}\Phi_{C,k+1}+\frac{\partial\Phi_{C,k+1}}{\partial r}\right)=0,\end{aligned} \tag{C7}$$

$$(k=N\ge 3)\ :\ \frac{N}{r}\Phi_{S,N}+\frac{\rho}{2}\left(-\frac{\partial\Phi_{S,N-1}}{\partial r}+\frac{N-1}{r}\Phi_{S,N-1}\right)=0, \tag{C8}$$

$$(k=N\ge 3)\ :\ -\frac{N}{r}\Phi_{C,N}-\frac{\rho}{2}\left(\frac{N-1}{r}\Phi_{C,N-1}-\frac{\partial\Phi_{C,N-1}}{\partial r}\right)=0, \tag{C9}$$

$$(k=N+1\ge 3)\ :\ -\frac{\partial\Phi_{S,N}}{\partial r}+\frac{N}{r}\Phi_{S,N}=0, \tag{C10}$$

$$(k=N+1\ge 3)\ :\ -\frac{N}{r}\Phi_{C,N}+\frac{\partial\Phi_{C,N}}{\partial r}=0. \tag{C11}$$

Note that both $\Psi_{S,1}$ and $\Psi_{C,1}$ are explicitly described in Eqs. (C1) and (C2) for the discussion about the choice of the retrieved variable. In what follows, we suppose that $N \ge 2$, but to modify the argument to $N < 2$ is trivial.

Even though the number of the Fourier components of the velocity potential has been reduced to make $F \le E$, there still remains non-trivial flows that satisfy Eqs (C1)-(C11). This is because these equations are differential equations along r, so non-trivial solutions are possible. The ambiguity arising from this fact can be solved by eliminating its solution, which is derived in what follows. From Eqs. (C10) and (C11),

$$\Phi_{S,N} = C_{S,N} r^N, \quad \Phi_{C,N} = C_{C,N} r^N, \qquad (C_{S,N}, C_{C,N} = \text{const.}). \tag{C12}$$

The flow represented by Eq. (C12) is non-rotational and non-divergent. Therefore, the wavenumber-N component of $\mathbf{V}_{\text{non}}$ cannot be constrained by the single Doppler measurement.[4]

By examining Eqs. (C6)-(C9) recursively to lower wavenumbers, we can understand that the ambiguity by the non-trivial solution is also associated with $\mathbf{V}_{\text{non}}$ down to the wavenumber 2. For example, from Eq. (C8), the general solution of $\Phi_{S,N-1}$ is its specific solution plus the general solution of the homogeneous equation (i.e., $-\frac{\partial \Phi_{S,N-1}}{\partial r} + \frac{N-1}{r}\Phi_{S,N-1} = 0$). The ambiguity is introduced by the latter, which is $C_{S,N-1} r^{N-1}$ ($C_{S,N-1}$ is an arbitrary constant). Likewise, the entire ambiguity takes the form of

$$\Phi_{S,k} = C_{S,k} r^k, \quad \Phi_{C,k} = C_{C,k} r^k, \quad \text{for} \quad 2 \le k \le N. \tag{C13}$$

The ambiguity for the wavenumber-1, from Eqs. (C4) and (C5), can be expressed as follows:

$$\Phi_{S,1} + \Psi_{C,1} = C_{S,1} r, \quad \Phi_{C,1} - \Psi_{S,1} = C_{C,1} r, \qquad (C_{S,1}, C_{C,1} = \text{const.}) \tag{C14}$$

The radial structure of $\Psi_{C,1}$ ($\Psi_{S,1}$) is determined by divergence $D_{C,1}(r')$ [$D_{S,1}(r')$] and the Green function $G_1(r;r')$, which is proportional to r at radii $r < r'$, in Eq. (26). Therefore, by vanishing any divergence at and outside the outermost radius of the radar observation [i.e., $D_{C,1}(r' \ge r_{m-1/2}) = 0$ or $D_{S,1}(r' \ge r_{m-1/2}) = 0$], we can remove the structure which is proportional to r of $\Psi_{C,1}$ ($\Psi_{S,1}$) in Eq. (C14):

$$\Phi_{S,1} = C_{S,1} r, \quad \Phi_{C,1} = C_{C,1} r. \tag{C15}$$

[4]The flow represented by the streamfunction for the wavenumber k, which is a proportional to r^k, is often introduced as one of incompressible potential flows around a stagnant point in textbooks of fluid dynamics (e.g., 2.7 in Batchelor 1967). The streamfunction for the wavenumber 1, which is a proportional to r, especially exhibits a horizontally uniform flow, related to the mean wind.

In substituting $\varPhi_{S,1}$ in Eq. (C15) into Eqs. (C1) and (C2), we obtain the following relationships:

$$\frac{\partial \varPsi_0}{\partial r} = \rho C_{S,1}, \tag{C16}$$
$$\frac{\partial \varPsi_0}{\partial r} = \frac{1}{\rho} C_{S,1}. \tag{C17}$$

From Eqs. (C16) and (C17), $C_{S,1} = 0$ is automatically satisfied without any constraints. Therefore, only $\Phi_{C,1}$ for the wavenumber-1 components requires the constraints. We discuss the better choice of the velocity potential for the wavenumber 1 in the retrieval. When we select $\Psi_{C,1}$ (and $\Psi_{S,1} = 0$) in the retrieval, from Eqs. (C1) and (C2) with Eq. (C14), we obtain

$$-\frac{\partial \Psi_0}{\partial r} + \rho \left(\frac{1}{r}\Phi_{S1} - C_{S,1} + \frac{\partial \Phi_{S1}}{\partial r} \right) = 0, \tag{C18}$$
$$\frac{1}{r}\Phi_{S1} - C_{S,1} + \frac{\partial \Phi_{S1}}{\partial r} - \rho \frac{\partial \Psi_0}{\partial r} = 0. \tag{C19}$$

From Eqs. (C18) and (C19), the solution for the axisymmetric structure is obtained:

$$\frac{\partial \Psi_0}{\partial r} = 0. \tag{C20}$$

Equation (C20) indicates that the axisymmetric flow doesn't have any interdependence and non-trivial flows if we select $\Psi_{C,1}$ in the retrieval and prescribe appropriate $C_{S,1}$ at the outermost radius ($r = r_{m-1/2}$). On the other hand, if we select $\Psi_{S,1}$ (and $\Psi_{C,1} = 0$) in the retrieval, from Eqs. (C3) with Eq. (C14),

$$-C_{C,1} - \frac{\partial \Phi_{C,1}}{\partial r} - \frac{1}{r}\Phi_{C,1} + \rho \frac{\partial \Phi_0}{\partial r} = 0. \tag{C21}$$

Equation (C21) indicates that the axisymmetric flows can have the ambiguity (i.e., $C_{C,1}$) even though we prescribe the ambiguity of $\Phi_{C,1}$ at the outermost radius. In contrast to the choice of $\Psi_{C,1}$, Eq. (C21) has no counterpart to eliminate the ambiguity. Thus, in the choice of $\Psi_{S,1}$, additional constraints are needed. We conclude that $\Psi_{C,1}$ in the retrieval is the better choice for the wavenumber-1 velocity potential.

The above argument indicates that we can eliminate the ambiguity associated with the non-trivial solution by introducing a constraint to fix all of $C_{S,k}$, $(k = 2, \cdots, N)$, and $C_{C,k}$, $(k = 1, \cdots, N)$. This can be done in various ways: for example, by specifying the values a priori at $r = r_{m-1/2}$,

$\Phi_{S,k,m-1/2}$, $(k = 2,\cdots,N)$, $\Phi_{C,k,m-1/2}$, $(k = 1\cdots N)$. Since knowledge about them are usually limited, one can simply set them to 0. In this case, asymmetric radial winds vanish at $r_{m-1/2}$. Although it is not needed, we can further impose $\partial\Phi_{S,k}/\partial r = \partial\Phi_{C,k}/\partial r = 0$ at $r_{m-1/2}$ to eliminate asymmetric tangential winds too. Although we have not conducted a systematic comparison, we expect that this additional constraint would reduce spurious signals when data quality is not very good. Alternatively, if sufficient external information is available, one can specify non-zero values to $\Phi_{C,k}$, $\Phi_{S,k}$, and their derivatives at $r_{m-1/2}$. This is especially recommended for $\Phi_{C,1}$, since it affects the axisymmetric tangential winds as shown in section 2e.

References

Batchelor, G. K., 1967: *An Introduction to Fluid Dynamics*. Cambridge University Press, 615 pp.

Bell, M. M., and W.-C. Lee, 2012: Objective tropical cyclone center tracking using single-Doppler radar. *J. Appl. Meteor. Climatol.*, **51**, 878–896, https://doi.org/10.1175/JAMC-D-11-0167.1.

Bell, M. M., M. T. Montgomery, and W.-C. Lee, 2012: An axisymmetric view of concentric eyewall evolution in Hurricane Rita (2005). *J. Atmos. Sci.*, **69**, 2414–2432, https://doi.org/10.1175/JAS-D-11-0167.1.

Cha, T.-Y., and M. M. Bell, 2021: Comparison of single-Doppler and multiple-Doppler wind retrievals in Hurricane Matthew (2016). *Atmos. Meas. Tech.*, **14**, 3523–3539, https://doi.org/10.5194/amt-14-3523-2021.

Cha, T.-Y., M. M. Bell, W.-C. Lee, and A. J. DesRosiers, 2020: Polygonal eyewall asymmetries during the rapid intensification of Hurricane Michael (2018). *Geophys. Res. Lett.*, **47**, e2020GL087 919, https://doi.org/10.1029/2020GL087919.

Dai, H., and Coauthors, 2021: Quasi-periodic intensification of convective asymmetries in the outer eyewall of Typhoon Lekima (2019). *Geophys. Res. Lett.*, **48**, e2020GL091 633, https://doi.org/10.1029/2020GL091633.

Houze, R. A., Jr., S. S. Chen, B. F. Smull, W.-C. Lee, and M. M. Bell, 2007: Hurricane intensity and eyewall replacement. *Science*, **315**, 1235–1239, https://doi.org/10.1126/science.1135650.

Houze, R. A., Jr., and Coauthors, 2006: The hurricane rainband and intensity change experiment: Observations and modeling of hurricanes Katrina, Ophelia, and Rita. *Bull. Amer. Meteor. Soc.*, **87**, 1503–1521, https://doi.org/10.1175/BAMS-87-11-1503.

Jou, B. J.-D., W.-C. Lee, S.-P. Liu, and Y.-C. Kao, 2008: Generalized VTD retrieval of atmospheric vortex kinematic structure. Part I: Formulation and error analysis. *Mon. Wea. Rev.*, **136**, 995–1012, https://doi.org/10.1175/2007MWR2116.1.

Kobayashi, S., and Coauthors, 2015: The JRA-55 Reanalysis: General specifications and basic characteristics. *J. Meteor. Soc. Japan*, **93**, 5–48, https://doi.org/10.2151/jmsj.2015-001.

Kossin, J. P., and W. H. Schubert, 2001: Mesovortices, polygonal flow patterns, and rapid pressure falls in hurricane-like vortices. *J. Atmos. Sci.*, **58**, 2196–2209, https://doi.org/10.1175/1520-0469(2001)058<2196:MPFPAR>2.0.CO;2.

Kossin, J. P., W. H. Schubert, and M. T. Montgomery, 2000: Unstable interaction between a hurricane's primary eyewall and a secondary ring of enhanced vorticity. *J. Atmos. Sci.*, **57**, 3893–3917, https://doi.org/10.1175/1520-0469(2001)058<3893:UIBAHS>2.0.CO;2.

Lai, T.-K., K. Menelaou, and M. K. Yau, 2019: Barotropic instability across the moat and inner eyewall dissipation: A numerical study of Hurricane Wilma (2005). *J. Atmos. Sci.*, **76**, 989–1013, https://doi.org/10.1175/JAS-D-18-0191.1.

Lee, W.-C., and M. M. Bell, 2007: Rapid intensification, eyewall contraction, and breakdown of Hurricane Charley (2004) near landfall. *Geophys. Res. Lett.*, **34**, L02 802, https://doi.org/10.1029/2006GL027889.

Lee, W.-C., P. R. Harasti, M. Bell, B. J.-D. Jou, and M.-H. Chang, 2006: Doppler velocity signatures of idealized elliptical vortices. *Terr. Atmos. Ocean. Sci.*, **17**, 429–446, https://doi.org/10.3319/TAO.2006.17.2.429(A).

Lee, W.-C., B. J.-D. Jou, P.-L. Chang, and S.-M. Deng, 1999: Tropical cyclone kinematic structure retrieved from single-Doppler radar observations. Part I: Interpretation of Doppler velocity patterns and the GBVTD technique. *Mon. Wea. Rev.*, **127**, 2419–2439, https://doi.org/10.1175/1520-0493(1999)127<2419:TCKSRF>2.0.CO;2.

Lee, W.-C., B. J.-D. Jou, P.-L. Chang, and F. D. Marks, 2000: Tropical cyclone kinematic structure retrieved from single-Doppler radar observations. Part III: Evolution and structures of Typhoon Alex (1987). *Mon. Wea. Rev.*, **128**, 3982–4001, https://doi.org/10.1175/1520-0493(2000)129<3982:TCKSRF>2.0.CO;2.

Lee, W.-C., and F. D. Marks, 2000: Tropical cyclone kinematic structure retrieved from single-Doppler radar observations. Part II: The GBVTD-simplex center finding algorithm. *Mon. Wea. Rev.*, **128**, 1925–1936, https://doi.org/10.1175/1520-0493(2000)128<1925:TCKSRF>2.0.CO;2.

Lee, W.-C., and J. Wurman, 2005: Diagnosed three-dimensional axisymmetric structure of the Mulhall Tornado on 3 May 1999. *J. Atmos. Sci.*, **62**, 2373–2393, https://doi.org/10.1175/JAS3489.1.

Montgomery, M. T., and R. J. Kallenbach, 1997: A theory for the vortex Rossby waves and its application to spiral bands and intensity changes in hurricanes. *Quart. J. Roy. Meteor. Soc.*, **123**, 435–465, https://doi.org/10.1002/qj.49712353810.

Muramatsu, T., 1986: The structure of polygonal eye of a typhoon. *J. Meteor. Soc. Japan*, **64**, 913–921, https://doi.org/10.2151/jmsj1965.64.6_913.

Murillo, S. T., W.-C. Lee, M. M. Bell, G. M. Barnes, F. D. Marks, and P. P. Dodge, 2011: Intercomparison of Ground-Based Velocity Track Display (GBVTD)-retrieved circulation centers and structures of Hurricane Danny (1997) from two coastal WSR-88Ds. *Mon. Wea. Rev.*, **139**, 153–174, https://doi.org/10.1175/2010MWR3036.1.

Schubert, W. H., M. T. Montgomery, R. K. Taft, T. A. Guinn, S. R. Fulton, J. P. Kossin, and J. P. Edwards, 1999: Polygonal eyewalls, asymmetric eye contraction, and potential vorticity mixing in hurricanes. *J. Atmos. Sci.*, **56**, 1197–1223, https://doi.org/10.1175/1520-0469(1999)056<1197:PEAECA>2.0.CO;2.

Shimada, U., and T. Horinouchi, 2018: Reintensification and eyewall formation in strong shear: A case study of Typhoon Noul (2015). *Mon. Wea. Rev.*, **146**, 2799–2817, https://doi.org/10.1175/MWR-D-18-0035.1.

Shimada, U., M. Sawada, and H. Yamada, 2016: Evaluation of the accuracy and utility of tropical cyclone intensity estimation using single ground-based Doppler radar observations. *Mon. Wea. Rev.*, **144**, 1823–1840, https://doi.org/10.1175/MWR-D-15-0254.1.

Shimada, U., M. Sawada, and H. Yamada, 2018: Doppler radar analysis of the rapid intensification of Typhoon Goni (2015) after eyewall replacement. *J. Atmos. Sci.*, **75**, 143–162, https://doi.org/10.1175/JAS-D-17-0042.1.

Tsujino, S., 2023: GVTD-X: Release version-1.1. Zenodo, https://doi.org/10.5281/zenodo.7656827.

Yamauchi, H., O. Suzuki, and K. Akaeda, 2006: A hybrid multi-PRI method to dealias Doppler velocities. *SOLA*, **2**, 92–95, https://doi.org/10.2151/sola.2006-024.